Chemically Reduced Graphene Oxide / Chitosan Hybrid; a Nanoscale "Fabric Starch"

CHITOSAN

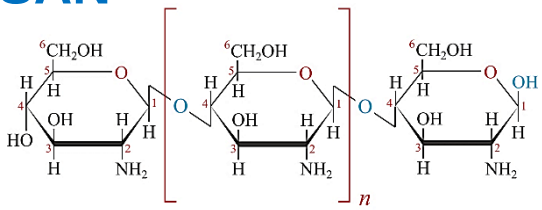

Ascorbic Acid

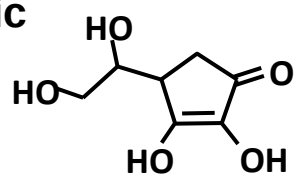

GO

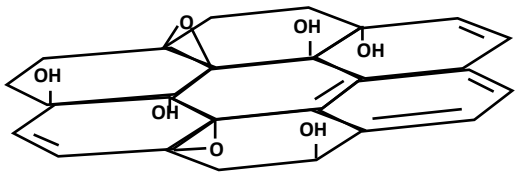

hybrid material

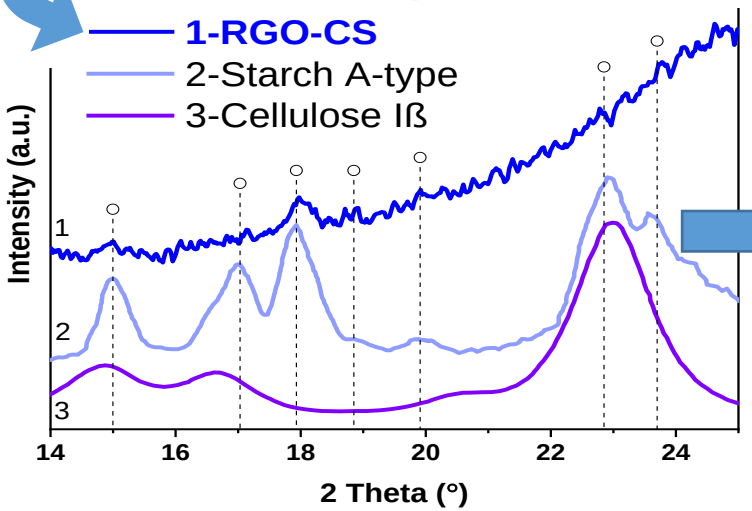

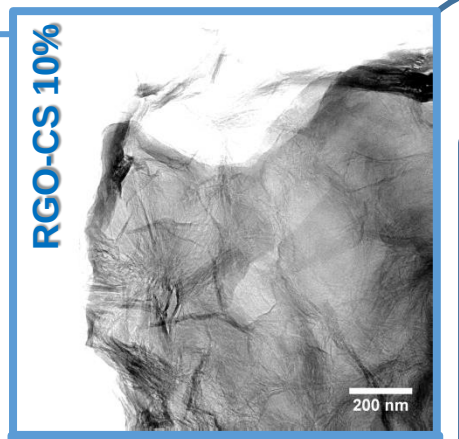

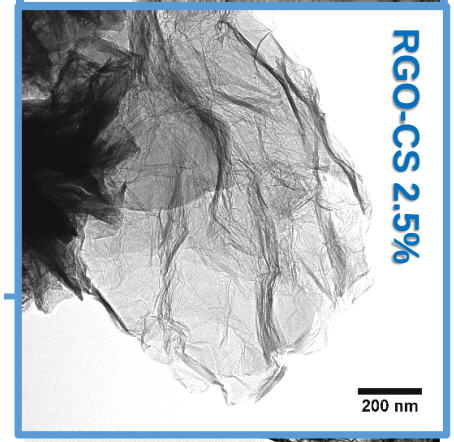

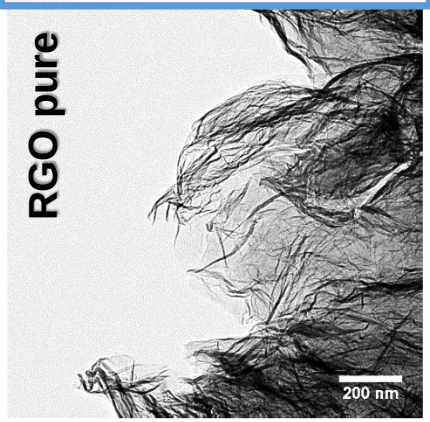

Less crumpling

Higher packing density & surface area

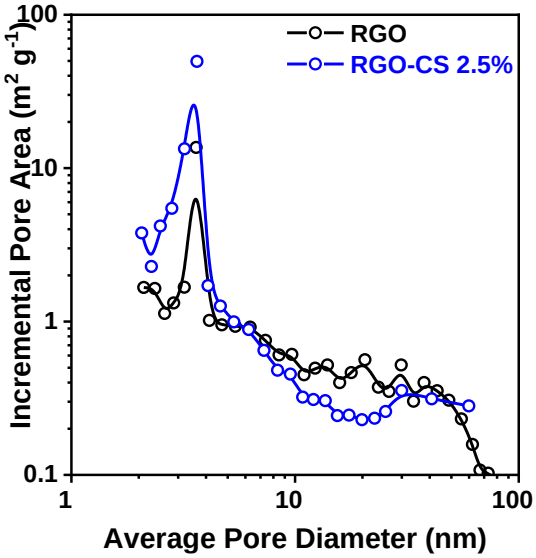

Starch like phase onto RGO sheets

Graphical Abstract *https://doi.org/10.1016/j.apsusc.2022.155229*

Chemically Reduced Graphene Oxide / Chitosan Hybrid; a Nanoscale "Fabric Starch"

Mazdak Hashempour[1], Mariangela Longhi[2], Luigi Brambilla[3], and Antonello Vicenzo[1,*]

[1] *Dipartimento di Chimica, Materiali e Ingegneria Chimica "Giulio Natta", Politecnico di Milano, Via Luigi Mancinelli 7, 20131, Milano, Italy*

[2] *Dipartimento di Chimica, Università degli Studi di Milano, Via Golgi 19, 20133 Milano, Italy*

[3] *Dipartimento di Chimica, Materiali e Ingegneria Chimica "Giulio Natta", Politecnico di Milano, Piazza Leonardo da Vinci 32, 20133 Milano, Italy*

* *Corresponding author*: antonello.vicenzo@polimi.it - +39 0223993140

Abstract

This work reports on the formation of reduced graphene oxide/chitosan, RGO/CS, (0.1–10 wt%) hybrids via L-ascorbic acid reduction of GO-CS aqueous suspensions. Hybrids at different synthesis steps and the constituent modifications are characterized by microstructural, spectroscopic and physical methods. CS undergoes chemical-structural changes, both by interaction with GO and in the course of the chemical reduction, so that eventually, whilst there is no evidence of CS presence in the final product, we find convincing proof of its transformation to a starch-like phase via a critical examination of XRD and ATR-FTIR analysis. Hybrids show significant modifications of composition, conductivity, apparent surface area and packing density vs. the pristine RGO. We elucidate more subtle effects, affecting stacking and packing behavior, by examining the capacitive storage behavior of hybrid electrodes. The electrochemical study highlights, at the best composition, a remarkable enhancement of specific/volumetric capacitance (up to 30% and 90% increase, respectively) and of rate behavior, compared to pure RGO. Overall, we show that the functioning of CS in hybrid formation can be explained through the reactive attachment of CS molecules onto RGO sheets, forming a starch-like phase, which stiffens graphene layers mitigating crumpling, and allowing a denser packing without re-stacking.

Keywords: Reduced graphene oxide, chitosan, hybrid, FTIR, supercapacitive behavior

1 Introduction

The graphene family has emerged as a promising material for a variety of applications shortly after its discovery [1]. What makes graphene attractive, particularly for electrical and electrochemical applications, is the combination of high electrical conductivity and high surface area [2–5]. Nevertheless, high throughput synthesis methods amenable to industrial production were shown to impair the intrinsic advantages of graphene. Synthesis of graphene oxide (GO) via chemical oxidation of graphite in strongly oxidizing environment [6,7], followed by chemical reduction [8] for the formation of reduced graphene oxide (RGO), is the best-established approach for mass production of graphene materials. However, the exceptional electrical conductivity of graphene [2] is seriously undermined by the structural and compositional damage induced by chemical oxidation [9]. Moreover, the full advantage of the high surface area of graphene, with theoretical values in the range of 2600 $m^2 g^{-1}$ [4,5,10], is not achievable in RGO due partly to incomplete exfoliation in the oxidation stage, and partly to agglomeration and re-stacking of the sheets during reduction [9,11]. The recovery of the electrical conductivity of GO through chemical reduction methods has been addressed with the use of effective reducing agents such as hydrazine [12] and L-ascorbic acid [13,14]. The observed conductivity is far below the value expected for graphene; still, it is high enough for most electrochemical applications, as an example. On the other hand, the issue of agglomeration and re-stacking of RGO sheets has been tackled via several strategies. Processing methods developed to minimize the irreversible re-stacking of RGO sheets include the synthesis of three-dimensional graphene networks [15], via hydrothermal self-assembly [16] or chemical cross-linking [17], the fabrication of graphene-carbon [18–20], graphene-metal [21], graphene-ceramic [22], graphene-polymer [23] hybrids or composites, and RGO surface modification by functionalization [24].

Chitosan (CS), an amino polysaccharide obtained from deacetylation of chitin exoskeletons of arthropods, has been studied for long, with a special focus on the properties that makes it appealing for biological, medical, agricultural, and environmental applications [25–27]. More recently, it has also attracted attention for electrochemical applications such as sensing [28] and energy storage [29]. Particularly, in the field of supercapacitors, the use of chitosan in development of active electrode materials is growing [30,31]. Nevertheless, most literature in this field reports about pyrolysis and activation of CS for the

production of activated carbon (AC) [32–42], which makes sense from the viewpoint of its abundance and cost. Examples of specific applications of CS for nano-scale engineering of porous supercapacitor electrodes, in particular based on graphene materials, are also reported [43–51]. Nevertheless, even in this latter group of works, the focus remains on CS as the major constituent and RGO takes the role of a modifier, by, e.g., fine-tuning the texture or enhancing the electrical conductivity. Sun et al. [43] prepared a CS-GO hydrogel by mixing and further processing individual suspensions of GO and CS, with a CS:GO mass ratio of 50:1. The prepared hydrogel underwent drying, carbonization and activation, leading to the formation of a CS-RGO based AC composite. The BET surface area of the AC composite was 1.5 times higher than the CS single component based AC, which, in turn, resulted in almost 50% improvement of the specific capacitance when used as supercapacitor active material. Similarly, Zhang et al. [44] prepared a CS-GO hydrogel, but with a lower CS:GO mass ratio of 4:1. The hydrogel was dried and carbonized but not activated, probably because of the lower content of CS compared with [43]. The CS-RGO composite showed a reasonable specific capacitance but poor rate capability. Gao et al. [45] used a microwave-assisted hydrothermal method to reduce CS:GO suspension of mass ratio 1:1, without further carbonization or activation process. The authors reported that inhibition of restacking and improved dispersion of RGO contributed synergistically to enhance capacitive performance, together with a pseudocapacitive contribution stemming from oxygen and nitrogen functional groups.

The opposite compositional paradigm, i.e., minor content of CS in an RGO–CS hybrid, has been studied for applications such as water treatment and sensing [52–54], and rarely, if ever, as an energy storage electrode material (Salleh et al. used 10 wt% CS as the binder for graphene based supercapacitor [55]). Tan et al. [56] reported the synthesis of GO quantum dots (GQDs)–CS nanocomposite having a reasonable supercapacitive performance after thermal treatment. However, notwithstanding the difference in synthesis and processing of GQDs and GO/RGO flakes, the precise composition of the composite is not reported in [56], while morphological analysis suggests that the CS phase may be the major constituent.

In the present work, we show that an RGO–CS hybrid can be synthesized by a simple wet chemical method consisting in the preparation of slightly acidic GO and CS suspensions, with a nominal content of CS varied from 0.1 to 10 wt%, followed by chemical reduction under reflux conditions..

There are two specific research objectives for this study. The first is to elucidate the interactions and modifications of CS and GO/RGO in the course of hybridization, which will affect the physicochemical, textural and morphological properties of the product. The second is, specifically, a comparative evaluation of the performance of such hybrids for electrochemical applications, and, more generally, a supplement investigation to corroborate and complement the first objective. Detailed assessment of the GO/RGO–CS hybridization in the aforementioned composition range and with the above goals has been rarely, if ever, reported. The mechanisms here disclosed by which CS modifies the RGO arrangement can be very insightful for research works addressing the tuning of microstructural and textural properties of RGO-based hybrids to improve specific, application-oriented performances. The hybrid shows promising characteristics towards enhanced porous structure and improved stability against re-stacking, through a non-trivial mechanism, i.e., stiffening of RGO layers and increase of the packing density. We use a combination of microstructural, physicochemical, spectroscopic and electrochemical characterization techniques to provide comprehensive insight into the interactions of RGO and CS, the hybridization process itself, and the behavior of hybrids as electrode material for capacitive charging in an aqueous environment. The outcome of this analysis suggests a complex pattern of surface interactions and chemical modifications leading to the covering by CS derivatives of RGO sheets. The CS derivative layer, on the one hand, allows a denser packing of RGO sheets and, on the other hand, stiffens individual RGO sheets, reducing wrinkling and large scale crumpling, thus modifying the balance between macro- and mesopores in favor of the latter.

2 Experimental

2.1 RGO–CS hybrid synthesis

GO was synthesized from synthetic graphite powder (<20 μm, Aldrich), based on the Tour's method [57,58]. After completion of the oxidation procedure, the product was thoroughly washed with deionized water to near neutral pH (>6), and maintained in the form of a suspension. The procedure of hybrid preparation was as follows. A 1 mg ml^{-1} molecular suspension of CS in deionized water was prepared by adjusting the pH to 3 with acetic acid and stirring for 12 h until a transparent solution was obtained. A 1 mg ml^{-1} GO suspension was prepared by diluting the original 12 mg ml^{-1} GO suspension. In a typical

hybridization procedure, the 1 mg ml^{-1} GO suspension was stirred and sonicated for 1 h, and then, the desired amount of the 1 mg ml^{-1} CS suspension was added under stirring, and thoroughly dispersed by probe sonication at room temperature. The added amount of the CS suspension varied in the range of 0.1 to 10 ml in order to get CS:GO ratios 0.001:1 to 0.1:1 (or, 0.1% to 10%). The mixture was stirred and sonicated at room temperature for one hour before chemical reduction. The chemical reduction consisted of addition of L-ascorbic acid (AA) at a AA:GO ratio 10:1, stirring for 1 h to assure complete dissolution of AA, and then refluxing at 95 °C for 1 h. During reduction, the initial light brown color of the suspension changed to black. By completion of the reduction, the suspension was filtered. The black RGO–CS precipitates underwent multiple washing-centrifugation-filtering steps until a neutral pH (>6) was obtained, and finally were dried at 80 °C for 12 h. For the purpose of comparison, a similar procedure was used to reduce GO in the absence of CS, ending up to a pure RGO powder. For the sake of simplicity in naming, reduced samples prepared from CS:GO ratios of 0.1%, 0.5%, 2.5% and 10%, are called RGO–CS 0.1%, RGO–CS 0.5%, RGO–CS 2.5%, RGO–CS 10%, respectively.

2.2 Material characterization

The prepared materials were characterized for crystalline phase analysis by X-ray diffraction (XRD) technique in Bragg–Brentano configuration using an 1830 PW Philips X-ray generator, equipped with a PW 3020 Philips goniometer and a PW 3710 Philips control unit. Morphological characterization of the samples was carried out using a scanning electron microscope, SEM (Zeiss EVO 50 EP). Small scale features of the morphology of RGO and RGO-CS hybrids were characterized by transmission electron microscopy (TEM), using a Philips CM200 FEG instrument equipped with a field emission gun with Schottky emitter, operated at 200 kV. Thermo-gravimetric analysis (TGA) was performed in air by using PerkinElmer Simultaneous Thermal Analyzer (STA 6000) at a heating rate of 10 °C min^{-1} up to 800 °C. N_2 adsorption-desorption isotherms were acquired at −196 °C (Micromeritics TriStar II 3020) after degassing at 90°C, to estimate the specific surface area (SSA) through the Brunauer–Emmett–Teller (BET) method as well as the pore size distribution via the Barrett–Joyner–Halenda (BJH) method. Infrared spectra of the solid samples in form of powder were obtained with a Nicolet Nexus FT-IR spectrometer coupled to an IR microscope Continuμm (Thermo Scientific) in attenuated total reflection

mode (ATR) using a Si tip single bounce slide-on ATR accessory. For each spectrum, 256 scans were collected with a resolution of 4 cm^{-1} in the spectral range 650–4000 cm^{-1}. Spectra reported in the figures are ATR corrected in order to make the spectral pattern more similar to an absorption pattern. Electrical conductivity of the compact powders was measured using a lab-made set-up consisting of a thick isolating PTFE die with a central circular hole and two cylindrical gold coated copper pistons (details available in our earlier work [20]). A variable load in the range of 2 to 150 N to the upper piston results in a compacting pressure over the powders in the range of 72 KPa to 5.27 MPa, under which the electrical resistance of the powders was measured. The electrical conductivity at each pressure was then calculated using Equation 1:

$$\sigma = \frac{l}{A.R} \quad (1)$$

where l is the powder column height, obtained by the displacement of the piston, A is the cross-section area of the piston, and R the measured resistance.

2.3 Electrode preparation and electrochemical characterization

Electrode preparation was based on a paste method [59] using PTFE as the binder and conductive carbon (CC, TIMCAL C-NERGY™ SUPER C65) as the conductivity promoter. The components were mixed in RGO–CS:CC:PTFE ratio of 82:10:8 in a mortar to form a paste which was then rolled on a PTFE plate resulting in a free-standing foil. The active layer was then cut in rectangular pieces of 7 mm × 7 mm and stuck onto a graphite current collector using conductive adhesive (DAG EB-021, LADD Research Industries). The apparent density of freestanding layers was measured before sticking onto the graphite foil, by precisely measuring the mass (Gibertini E154 microbalance with an accuracy of 0.1 mg), the thickness (20 μm resolution calipers) and the area (ImageJ processing of the scaled picture of the samples with an approximate resolution of 2.5×10^{-3} cm^2).

Electrochemical measurements were carried out in 1 M Na_2SO_4 electrolyte, at room temperature, using a ModuLab® XM ECS potentiostat / galvanostat system (Solartron Analytical XM PSTAT 1 MS/s), equipped with a frequency response analyzer (Solartron Analytical XM FRA). A three-electrode set up

was used for electrochemical characterization, consisting of RGO–CS electrodes as the working, a platinum foil as the counter, a 3.5 M KCl filled calomel probe as the reference electrode (all the results are nevertheless reported with respect to the standard hydrogen electrode, SHE, where E_{SCE} = +250 mV_{SHE}).

The electrodes were tested by cyclic voltammetry (CV) and electrochemical impedance spectroscopy (EIS). CV tests were carried out over the potential range 0 to 1 V_{SHE} and at five different scan rates, 1, 5, 20, 50 and 100 mV s^{-1}. The specific capacitance was calculated according to Equations 2 and 3:

$$C_g = \frac{1}{2} \times \frac{\oint IdV}{\nu \, \Delta V \, m} \quad (2)$$

$$C_v = \frac{1}{2} \times \frac{\oint IdV}{\nu \, \Delta V \, Vol} \quad (3)$$

where C_g is the gravimetric capacitance, C_v is the volumetric capacitance, $\oint IdV$ is the area enclosed in the voltammogram, ν is the scan rate, ΔV is the potential window, m and Vol are the paste electrode mass and volume, respectively.

EIS measurements were performed at the open circuit potential (OCP) using an AC excitation signal of 10 mV amplitude, in the frequency range from 100 kHz to 5 mHz, sampling 10 points per decade.

3 Results and discussion

3.1 Electron Microscopy

Fig. 1 shows SEM images of as-prepared RGO and RGO-CS hybrids, as well as of as-received CS powder. While the RGO powder shows mostly relatively large, irregular platelets – presumably stacks of numerous RGO sheets (Fig. 1a) – RGO–CS hybrids (Fig. 1b–d) show smaller aggregates with a granular and relatively fluffy morphology. As-received CS powder, in Fig. 1e, consists of rather coarse lumps of material, which are obviously untraceable in the hybrids.

The morphology of the hybrids was examined also by TEM, as shown by images of selected samples in Fig. 2, in the search of evidence of the presence of CS on RGO at the nano-scale. Neither the high magnification (Fig. 2c and e) nor the high resolution (Fig. 2d and f) TEM micrographs of RGO–CS

hybrids reveal peculiar features traceable to the presence of CS directly, when contrasted with the corresponding RGO images (Fig. 2a and b). Also the selected area electron diffraction patterns (SAED, insets of Fig. 2a, c and e) of the samples show only the (002) and (101) crystalline planes of graphitic carbon. Regardless of works with CS as the by far major constituent (e.g., [43,44]), which are not comparable with our work, previous reports either suggest [52–54] or reveal [60] the absence of morphological contrast enabling phase distinction, as in the present work, or recognize different morphological features that are assigned to RGO/GO and CS (e.g., [45,55]). Moreover, there are instances where the morphological identification of different phases appeared to be possible only at a certain stage of processing [56] or only in a range of experimental conditions [61]. Overall, the heterogeneity and multiplicity of reports on the morphology of hybrids and their conflicting outcome on the phase contrast in RGO–CS or GO–CS hybrids make these results inconclusive. On the other hand, it is an important remark of the present work the distinction between RGO and RGO–CS hybrids from a different viewpoint, that is, the degree of distortion and wrinkling of individual sheets, which apparently decreases with increasing CS content (compare Fig. 2a with Fig. 2c and e). Arguably, RGO-CS hybridization appears to have a stiffening effect on RGO sheets, greatly reducing their otherwise prompt tendency to corrugation. We can argue, then, that this effect implies the formation of a hybrid structure through supposedly strong molecular/atomic scale interactions. Additional characterization was conducted to evaluate this conjecture.

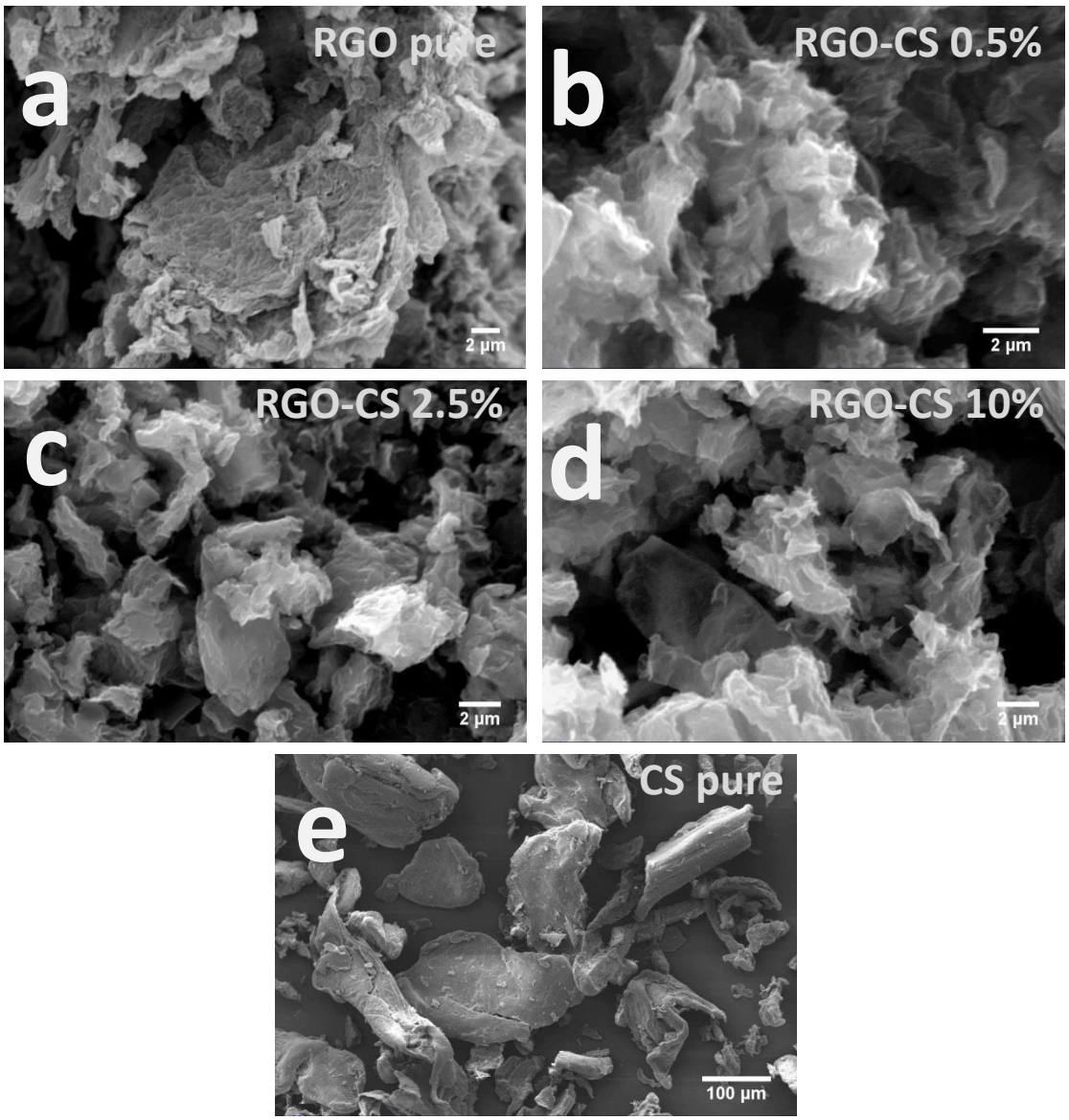

Fig. 1. (a-e) SEM micrographs of RGO, RGO–CS 0.5%, RGO–CS 2.5%, RGO–CS 10% and CS powders, respectively.

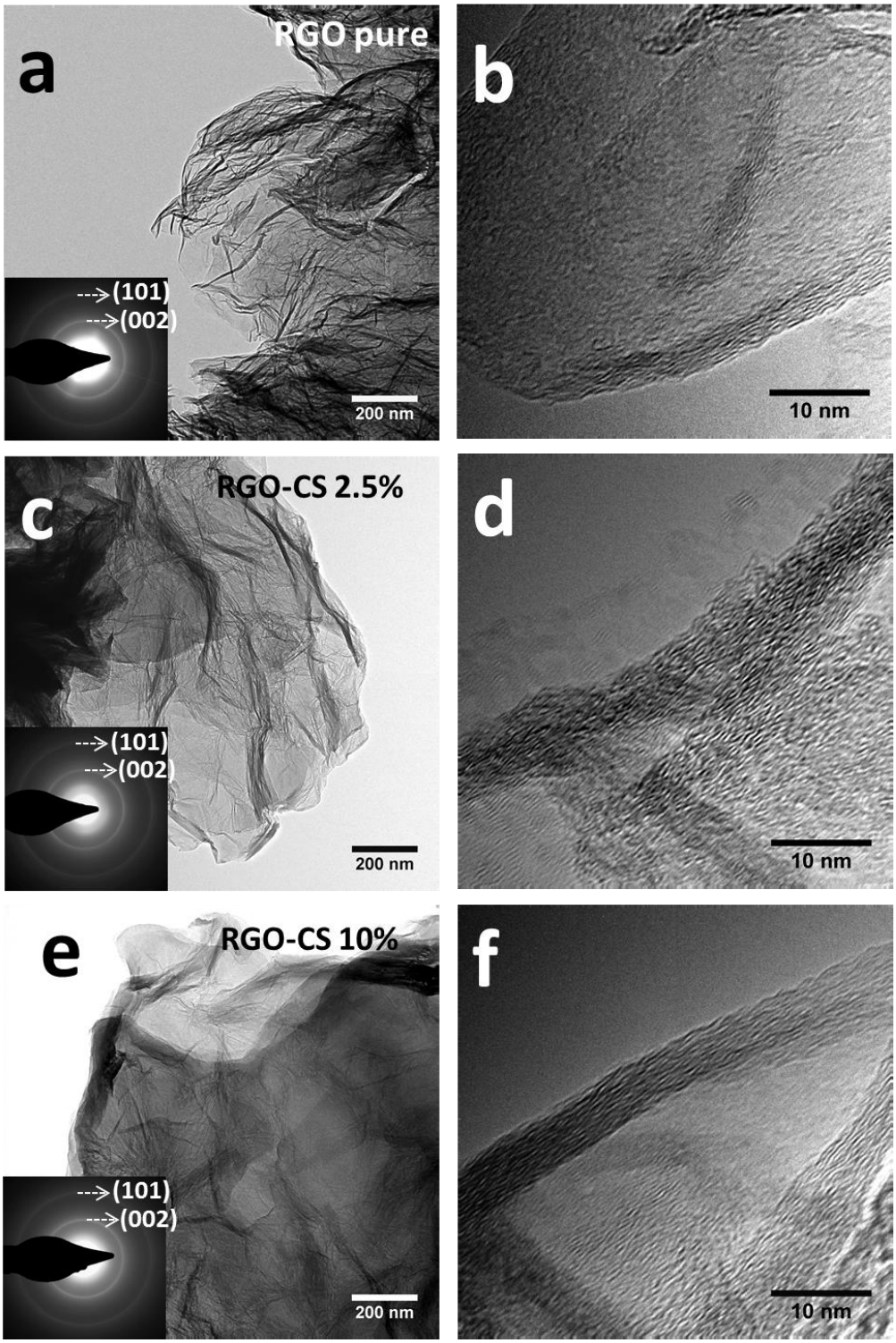

Fig. 2. TEM micrographs of RGO, RGO–CS 2.5% and RGO–CS 10%, respectively. Insets show the SAED patterns of the corresponding samples.

3.2 XRD

Fig. 3a compares the XRD patterns of RGO and RGO–CS 10% samples, showing in addition patterns of pristine graphite, GO and CS for reference purpose. Patterns of hybrids at lower CS content are not shown, since only for the latter composition we could get significant evidence from XRD analysis. The evolution of the graphite crystalline structure – as revealed by the (002), (100) and (101) reflections of hexagonal graphite belonging to the $P6_3/mmc$ space group [62] (at 2θ=26.543°, 42.321° and 44.518°, respectively); and by the low intensity (101) and (012) peaks of rhombohedral graphite belonging to the $R\bar{3}m$ space group [63] (at 2θ=43.454° and 46.321°, respectively) – in the course of its oxidation to GO – with the main peak appearing at 2θ=10.40° due to the introduction of oxygen functional groups in between (002) planes – has been articulated in previous reports, e.g. [20,64]. The disappearance of the characteristic GO peak at 2θ=10.40° and the reappearance of graphite features (broad peaks at about 2θ=25° and 43°) in RGO and RGO–CS hybrid suggests that the L-ascorbic acid reduction of GO was effective in the removal of oxygen groups. Only small differences emerge between the XRD patterns of RGO–CS 10% and RGO in Fig. 3a in the form of minor peaks in the 2θ range 15–25°, in particular at about 15° and 18°. Since these peaks do not match with the known pattern of CS [65,66], the presence of unmodified CS in the hybrid can be discarded, at least within the limits of XRD sensitivity, and in agreement with the analogous evidence of SEM analysis. Conversely, we remark that these peaks have a significant match with the crystalline patterns of basic carbohydrate polymers ($C_m(H_2O)_n$), i.e., cellulose and starch. Among different polymorphs of cellulose, cellulose Iβ shows a partial peak matching with RGO–CS 10%, precisely by the small reflection at 15° corresponding to the $(1\bar{1}0)$ plane [67]. Although there may be other minor peaks of cellulose Iβ overlapping with RGO–CS features (e.g., the hardly visible (111) plane coinciding with the feature at 18.9°), the absence of diffraction signals corresponding to the main reflections of cellulose Iβ, such as (110) and (200) planes at around 16.8° and 22.8°, respectively (Fig. 3b), rules out any chance of its presence in the sample. On the other hand, A-type starch (the type dominant in cereals [68]), shows a surprising match not only with the two particular features of RGO–CS 10% at 15° and 18°, but also with other still smaller features at 17°, 18.9°, 19.9°, 22.8° and 23.7°. Imberty et al. [69] assigned an orthorhombic-like unit cell to the crystalline part of A-type starch in which – quoting from the abstract – "twelve glucose residues are located in two left-handed, parallel-

stranded double helices packed in a parallel fashion". In such an orthorhombic-like lattice, the planes corresponding to the peaks at 15.0°, 17.0°, 18.0°, 18.9°, 19.9°, 22.8° and 23.7°, are (112), (103), (121), (211), (004), (123) and (213), respectively (according to the orthorhombic-like lattice reported in the ICDD 00-043-1858).

Starch and chitosan are polysaccharides with a similar backbone, the difference being in the plane α-(1→4)-linked D-glucose units of starch in contrast to the randomly distributed β-(1→4)-linked D-glucosamine and N-acetyl-D-glucosamine units of chitosan. Accordingly, the structural arrangement of chitosan into a pseudo-starch phase would require specific molecular interactions with the GO surface and its modification, notably the progress of deacetylation, in the course of the reaction procedure. In the attempt to gather further evidence in support of this hypothesis, we used ART-FTIR to study the hybridization process at different stages (Fig. 4a).

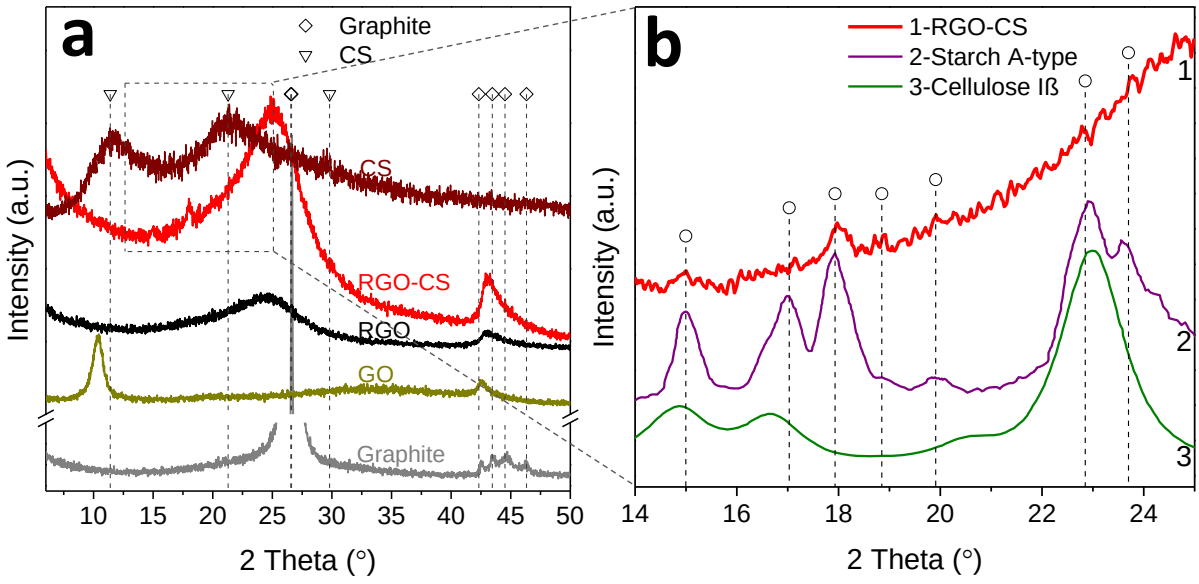

Fig. 3. (a) XRD patterns of graphite control sample, GO, RGO, RGO–CS 10% and CS, (b) zoom-in view of the 14–25° region of the RGO–CS 10% XRD pattern, overlaid with (intensities are not comparable) reference patterns of cellulose Iβ (adopted from [67]) and A-type starch (adopted from [69]).

3.3 ATR–FTIR

Spectra were collected from GO and CS dried powders, as parent constituents of the hybrids. To monitor the possible modifications of the material during the mixing and reduction processes, spectra were collected at different processing stages as pointed out in the following. Expectedly, the appearance of

spectral features associated with the hybrids is the clearer the higher is the content of pristine CS in the hybrid, and this is the reason why only the spectra of the hybrid with the highest CS concentration (i.e., 10 wt%) are shown in Fig. 4.

Hybrid samples were analyzed at the following stages: a) after the mixing procedure, but before reduction (GO–CS); b) after mixing and incomplete reduction (so-called premature RGO–CS, or in brief, pre-RGO–CS), achieved using a lower concentration of AA (AA:GO ratio 3:1), a lower temperature (90 °C) and a shorter time (immediate quenching to 25 °C after reaching the set temperature); c) after mixing and complete reduction (RGO–CS). Additionally, pure RGO was analyzed after complete reduction as the CS-free reference.

The ATR–FTIR spectrum of GO (green line, for reference to color images throughout the text, the reader is referred to the electronic version of the article) is characterized by the strong and broad bands in the O–H stretching range (3600-3000 cm^{-1}), typical of this material [70]. The very weak C–H stretching band at relatively low wave numbers (around 2800 cm^{-1}) may be attributed to the presence of aldehyde functional groups, considering the carbonyl stretching vibration in the region 1750–1700 cm^{-1} [71]. Carboxylic acid groups and derivatives account for most of the spectral features. Carboxylic anhydride is revealed by the (lower intensity) symmetric C=O stretching band at 1819 cm^{-1} coupled with the (higher intensity) asymmetric C=O stretching at 1733 cm^{-1} [72,73]. Carboxylate anions, COO^- , formed supposedly by partial deprotonation of carboxylic acids due to multiple washing, is revealed by the asymmetric $\overset{\cdots}{O}–C–\overset{\cdots}{O}$ stretching at 1619 cm^{-1} and the symmetric $\overset{\cdots}{O}–C–\overset{\cdots}{O}$ stretching in the range 1420–1300 cm^{-1} [74,75], where the GO spectrum however shows a broad and featureless absorption region. Carboxylic acid groups, COOH, are revealed by the C=O stretching in the 1730–1715 cm^{-1} range, accompanied with the O–H out-of-plane bending at 980 cm^{-1}, the C–O stretching at about 1220 cm^{-1} and the C–O–H in-plane bending at 1420 cm^{-1}, notwithstanding the broadness of the spectral features in these regions. The most intense spectral features of GO, grouped in the range 1250–1000 cm^{-1}, can be ascribed to etheric groups, particularly ethers aggregated at the edges of defects, which vibration bands, e.g., at 1150 cm^{-1}, 1113 cm^{-1} and 1041 cm^{-1} for the asymmetric C–O–C stretching mode, will vary remarkably depending on the number of groups accumulated and the defect type [76,77]. In addition to ethers, the presence of epoxide

groups is evidenced by the C–O–C bending motion at 879 cm^{-1} and asymmetric stretching at about 1300 cm^{-1}, which is shadowed by the broad spectral feature ranging from 1450 to 1250 cm^{-1}.

The spectrum of pristine CS powder (brown line) was acquired and analyzed as a reference for the interpretation of GO–CS and RGO–CS hybrids. The small bands in the range 3360–3293 cm^{-1}, floating over the typical broad O–H stretching range (3600–3000 cm^{-1}) of CS [78], are indicative of the overlap of N–H stretching modes of a primary amine and a secondary amide [79], in the NH_2 group of the D-glucosamine (deacetylated unit of CS) and the N-acetyl-D-glucosamine (acetylated unit of CS), respectively. The presence of both groups CH_2 (revealed by symmetric and asymmetric C–H stretching in the range 2920–2874 cm^{-1}, and symmetric bending at 1420 cm^{-1}, downshifted by the presence of C–O bonds of the hydroxyl group [80–85]) and CH_3 (revealed by symmetric and asymmetric C–H stretching in the range 2920–2874 cm^{-1}, the asymmetric bending at 1458 cm^{-1} and the symmetric bending – the so-called umbrella motion – at 1375 cm^{-1}) is evident in the hydroxymethyl (– CH_2–OH) and N-acetyl-D-glucosamine units of CS, respectively. Note that in the overlapping of C–H stretching vibrations of CH_2 and CH_3 groups, the contributions of the latter always appear at higher wavenumbers. All the three amide bands are recognized in the CS spectrum: amide I at 1651 cm^{-1} corresponding to C=O stretching weakly coupled with C–N stretching and N–H bending; amide II at 1590 cm^{-1} corresponding to the strong coupling of N–H bending with C–N stretching; and amide III at 1318 cm^{-1} originating from N–H in plane bending coupled with C–N stretching and from minor influences of C–H and N–H bending vibrations [86–90]. Moving to lower wavenumbers a variety of C–O bands are observed within 1250–950 cm^{-1}. The two bands at 1150 cm^{-1} and 992 cm^{-1} are attributed to asymmetric and symmetric stretching, respectively, of the C–O–C bridge between two adjacent glucosamine units, the so called β–(1,4) glycosidic linkage in CS chain [53,80–83,90–96]. There is not unanimous consent in the literature on the assignments of the other bands in the same region, at 1066 and 1030 cm^{-1}, being attributed to either endo– or exocyclic C–O stretching modes.

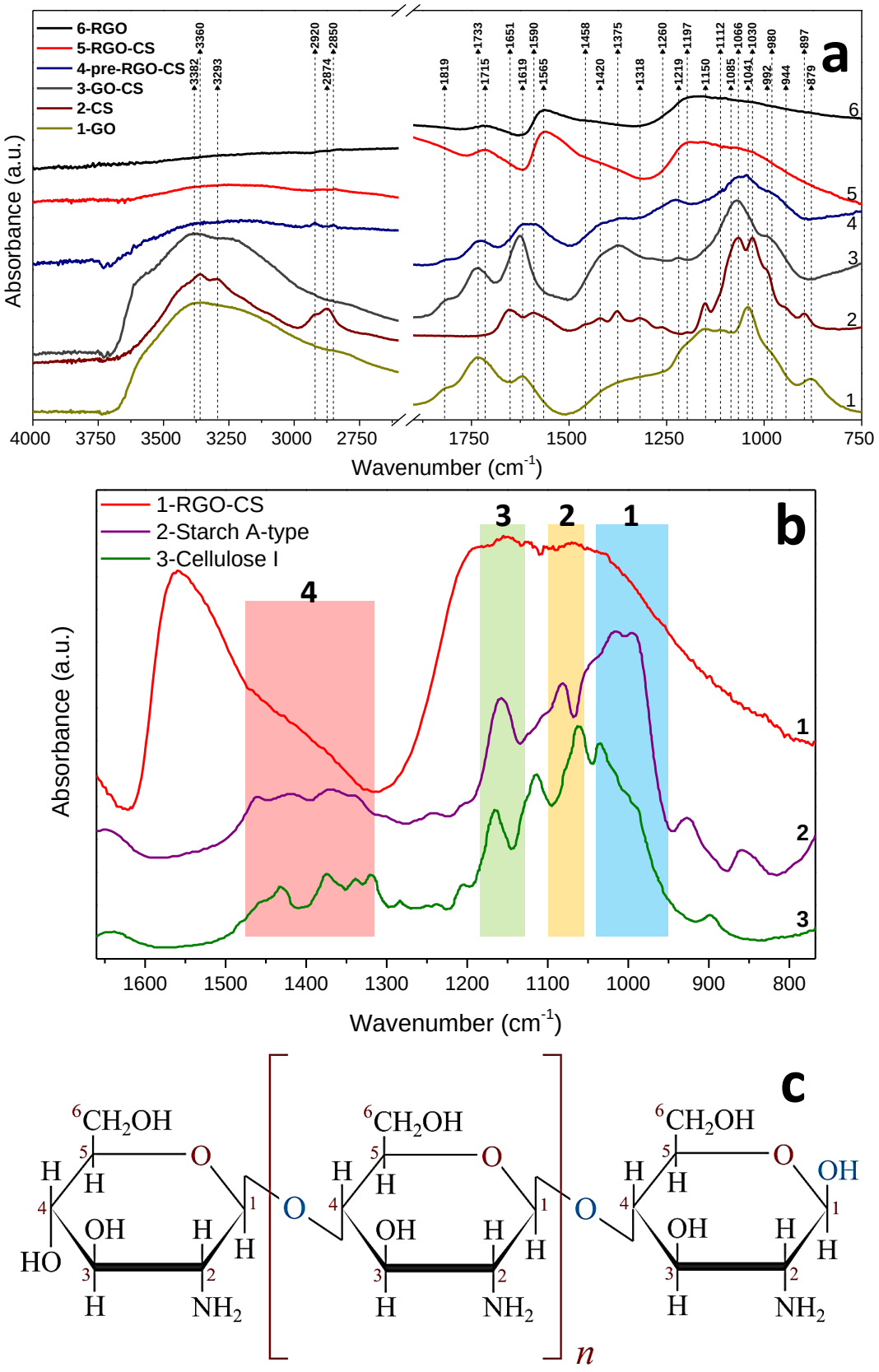

Fig. 4. (a) ATR-FTIR spectra of the GO, CS, GO–CS, pre-mature RGO–CS, RGO–CS and RGO samples, (b) zoom-in view of the fingerprint region of RGO–CS compared with A-type starch (adopted from [97]) and Cellulose I (adopted from [98]). Rectangles numbered 1–4 represent four spectral zones discussed in the text, and numbers at the right side of the curves represent the legend information. For the color version of this image the reader is referred to the electronic version of the article. (c) The molecular structure of fully deacetylated chitosan; β-(1→4)-linked D-glucosamine.

In particular, symmetric and asymmetric C–O–C stretching modes inside the pyranose ring, respectively at 1030 and 1066 cm^{-1}, are examples of the former [82,85,91], while C–O stretching vibrations primarily of the alcohol groups account for the latter [99,100]. Other features of the CS spectrum include the out-of-phase stretching of the pyranose ring at 897 cm^{-1} [80–83], the out-of-plane bending of the hydroxyl group at 944 cm^{-1} and its other deformation at 1197 cm^{-1}, and the C–H bending at 1260 cm^{-1} [80,82,98].

The first point noticed in the spectrum of GO–CS (grey line) is the strong reduction –almost to disappearance – of the amide I, II and III bands, observed in the CS spectrum at 1651 cm^{-1}, 1590 cm^{-1} and 1318 cm^{-1}, respectively. Noteworthy, in the spectrum of physically mixed GO and CS dry powders (not shown here), the amide bands are present. We infer therefore that amide transformation and interaction between GO and CS during the wet mixing procedure (suspension mixing) is responsible for the lowering or vanishing of the amide bands. We can think of two possible paths for this modification; (a) the advancement of deacetylation of the hydrolyzed CS upon mixing with GO suspension, and (b) interactions of GO and CS through the N site of the acetylated unit of CS. In addition to the disappearance of the C=O stretching of amide I, the weakening and broadening of both symmetric and asymmetric CH_3 bending motions as well as of the N–H stretching whit respect to CS support this interpretation. The other part of the GO–CS spectrum with remarkable modifications is the C–O region, showing only three bands, namely, 1153, 1070 and 980 cm^{-1}. Two of these bands, namely, 1153 and 980 cm^{-1}, correspond to β–(1,4) glycosidic linkage, as discussed in the case of CS spectrum. Both bands are greatly reduced in intensity, first, for the relatively low concentration of CS in GO–CS, but also because the glycosidic linkage is primarily a characteristic of the polymer and thus, the interaction of CS with GO after hydrolysis and, arguably, breakdown of this linkage, will involve oligomer fragments consisting of relatively few D-glucosamine units. The relatively stronger signal and the slight red-shift of the 980 cm^{-1} band is believed to be caused by its overlap with the O–H out-of-plane bending of the carboxylic acid originating from GO. The 1070 cm^{-1} band of GO–CS does not totally coincide with C–O bands of the CS (1066 cm^{-1}), or the aggregated edge ethers of GO (1041 cm^{-1}). This fact, along with the absence of C–O–C bending mode of epoxides (879 cm^{-1} band of GO), suggests that edge ethers and basal epoxides of GO served as linking sites to the CS mono/oligomers. The counter-site of such a linkage on CS, in addition to the N site discussed earlier, could be a C site on the pyranose ring, such as: (a) C-3 of CS, by

dehydroxylation of this carbon in its interaction with ethers/epoxides on GO; or (b) C-1 or C-4 of CS, through the replacement of the glycosidic linkage between CS monomers with a new linkage between CS and ethers/epoxides on GO (see Fig. 4c). The formation of such C_{GO}–O–C_{CS} linkage can firstly justify the vanishing in the hybrid spectrum of the out-of-phase pyranose ring stretching (observed at 897 cm^{-1} for CS), due to multiple point connection of the CS fragments to the GO sheets in the form of molecular patches, which have less chance for collective vibrations. Secondly, such a C_{GO}–O–C_{CS} bonding would obviously have a vibration band (1070 cm^{-1}) different from the C–O bands on CS (1030 and 1066 cm^{-1}). Changes in other parts of the GO–CS spectrum are minimal and share common features with either the CS or GO spectrum, including indicator bands of carboxylate anion, carboxylic anhydride, carboxylic acid, symmetric bending of both CH_2 and CH_3, and O–H stretching region.

The spectrum of pre-RGO–CS (navy blue line) reveals, in the first place, the robustness of the AA reducing effect, reflected by the strong decrease in the O–H region (3600-3000 cm^{-1}) as well as the reduced intensity of the C=O bands in the 1850–1550 cm^{-1} region. Reappearance of the C–H stretching bands, in spite of their apparent absence in the GO–CS, demonstrates their shielding by O–H groups of GO before reduction. More intense CH_2 related bands (C–H stretching bands at 2920 cm^{-1} and 2850 cm^{-1} as well as the scissors motion at 1420 cm^{-1}) compared with CH_3 (C–H stretches at 2952 cm^{-1} and 2875 cm^{-1}, and the umbrella motion at 1375 cm^{-1}) further supports the assumption of a gradual progress of CS deacetylation in the hybrid. The amide bands remain absent in the pre-RGO–CS, similar to GO–CS. Actually, in the latter sample, the band at 1590 cm^{-1}, which overlaps with the amide II band in CS, could be attributed to the emergence of skeletal C–C vibrations of reduced GO (band at 1565 cm^{-1} in RGO-CS), with a slight blue shift. In the C–O region, the glycosidic linkage bands at 1153 and 980 cm^{-1} are further reduced, not to say eliminated. From this analysis, we infer that the polymeric character of chitosan units attached to GO sheets decreases more and more with the progress of reduction. The C–O region (1070–1030 cm^{-1}) seems to show the reappearance of a doublet, that we arguably understand as asymmetric and symmetric stretching bands of the newly formed C_{GO}–O–C_{CS} bonds. Complementarily, we can say that the vibrations in the 1070–1030 cm^{-1} region relate to the saccharide residues formed by addition of CS. The indicator bands of carboxylate anion, carboxylic anhydride and carboxylic acid are still present in the pre-RGO–CS. By the progress and completion of the reduction treatment, substantial removal of most

functional groups is achieved, as revealed by the spectrum of RGO–CS (red line) and more clearly evidenced in that of RGO (black line). The large hump in the 3600–3000 cm^{-1} region of O–H and N–H stretching is significantly depressed in RGO-CS – while almost flattened in RGO – and C–H stretching bands are hardly visible. Marker bands of carboxylic anhydride at 1819 cm^{-1} and of carboxylate anion at 1620 cm^{-1} are not visible anymore and only the C=O stretching at 1715 cm^{-1} survived the strong reduction. The asymmetrically shaped band at 1565 cm^{-1} is assigned to the vibrations of condensed sp^2 carbon atoms; no sign of CS amide bands could be observed in RGO–CS. The most noticeable difference between RGO–CS and RGO is in the C–O region, where a very broad hump appears in the former and lacks in the latter. For a closer look, the fingerprint region is magnified in Fig. 4b, where shaded rectangles highlight wavenumber ranges of the RGO–CS spectrum, as follows: (1) 1040–950 cm^{-1}, (2) 1100–1050 cm^{-1}, (3) 1175–1125 cm^{-1}, and (4) 1475–1325 cm^{-1}. Since according to XRD results (Fig. 3b), A-type starch or, less likely, cellulosic species were identified as possible phases formed in RGO–CS hybrids, the reference FTIR spectra of these two species, namely A-type starch [97] and cellulose I [98,101], are overlapped with that of RGO–CS in Fig. 4b. The ranges 1 and 3, which correspond to C–O–C glycosidic linkage bands for both A-type starch [95,102] and cellulose I [80,94,95], show a better match of the A-type starch spectrum with RGO–CS, particularly in the range 1, where without the contribution of a relatively strong band in the minor constituent (i.e., the 994 cm^{-1} band of the starch), it would be hard to explain the evident shoulder in the RGO–CS spectrum. Therefore, while the glycosidic linkage bands of the original CS at 1153 and 980 cm^{-1} are decreasing in the course of hydrolysis, and by interaction with GO and reduction, it appears that saccharide species thereby emerging can reassemble on the surface of GO/RGO giving rise to structures with a spatial order similar to that observed in A-type starch. The structure of the pure A-type starch is composed of six left-handed double helices, wherein the pitch of the helices (i.e., 2c=2.138 nm) is affected – among other factors – by the quality of the glycosidic linkages, and the packing of the double helices (i.e., interstrand spacing corresponding to the unit cell parameters, a=2.124 nm and b=1.172 nm) is under the strong influence of a compact network of hydrogen bonds involving the primary and secondary hydroxyl groups of the glucose units [69,103]. It is inferred accordingly, that the lost β–(1,4) glycosidic linkages of the CS polymer are partially restored under a different configuration, namely, α-(1→4) linkages, upon collective deposition of the monomers

on GO. Such linkages not only justify the features observed in zones 1 and 3 of the RGO–CS spectrum (Fig. 4b), but also account for the crystallinity of the RGO-CS hybrid (micro-features in Fig. 3b). On the other hand, the evaluation of range 2 does not provide a clear clue about the match of the spectral feature of RGO–CS (1070 cm^{-1}) with either A-type starch (1081 cm^{-1}) or cellulose I (1060 cm^{-1}). Interestingly, since this band is already seen in the GO–CS spectrum (see Fig. 4a), it appears as a distinct feature of the interaction between RGO/GO–CS. It was discussed earlier that the formation of a C_{GO}–O–C_{CS} linkage through the interaction of ether/epoxide sites of GO with either dehydroxylated C-3 site of CS or a broken glycosidic linkage (C-1 or C-4 sites of CS) could generate a distinct vibration band not observed in CS. It is important to note that the C–O band of A-type starch at 1081 cm^{-1} has contributions from C–O–H deformations [104] and, therefore, perturbations in the intrinsic hydroxyl atmosphere and hydrogen bonding network of the pure phase could bring about modifications in the crystalline structure of the polymer, in particular, the packing of the double helices (i.e., a and b parameters of the unit cell). It is plausible therefore to assume that, whatever the specific interaction underlying the formation of the C–O band at 1070 cm^{-1} of RGO–CS, the resulting phase is a pseudo-A-type starch phase with molecular and structural peculiarities. Finally, a broad hump with very weak – yet non-zero – intensity appears in zone 4 of RGO–CS, which corresponds to various C–H deformations. Both A-type starch and cellulose I may be responsible for such weak bands of C–H deformations, particularly through their CH_2 moieties.

In brief, we conclude that the so-called RGO–CS hybrid is indeed composed of molecular islands of oligosaccharides sticking onto the graphene sheets, formed through the transformation of CS to a pseudo-A-type starch in the course of the thermochemical reduction, due to simultaneous deoxygenation, deacetylation and reactive attachment onto RGO. Accordingly, we will use the abbreviation CS^* from here on to refer to “Chitosan transformed to Starch-like phase”, whenever we intend to emphasize the differences between this species and the initial chemical, CS. Formation of starch by a deacetylation process is not unreported, though previous studies refer to different precursors and different synthesis routes [105–109].

3.4 Physical properties

Further characterization addressed physical properties and composition of the hybrids, namely CS* content, combustion temperature (Fig. 5a), apparent volumetric mass density (sometime referred to as packing density for porous or non-consolidated materials [110], Fig. 5b) and the electrical conductivity (Fig. 5c-e), looking for additional evidence about the hybridization process and its effects on RGO properties.

Whereas by mass measurements before and after synthesis of RGO, we can calculate an apparent yield ($\frac{mass\ of\ RGO}{mass\ of\ GO}$) of 53.7±1% for the AA reduction of GO, this approach cannot be applied to the assessment of the CS* content in the hybrid samples for the following reasons: (1) the yield of GO→RGO changes in the presence of CS; (2) the CS mass also changes during the hybridization process. Accordingly, we used thermal analysis in the attempt to overcome this issue. Since only the highest CS concentration could provide adequate resolution to attempt a reliable quantitative analysis, we report TGA and DTA results for the RGO and RGO–CS 10% sample, as shown in Fig. 5a. Both materials show a zero residue after burning completion (TGA curves, solid lines), demonstrating the absence of mineral contaminants. Moreover, both samples show a similar 4% mass loss by 100 °C, due to removal of adsorbed water. The combustion wave sets off at 450 °C for RGO, preceded by a 20% mass loss due to residual oxygen functional groups not completely removed during AA reduction [59]. The combustion onset for RGO–CS is slightly higher, at 480 °C, and the mass loss over the interval 100 to 480 °C is 8% larger than for RGO. Additionally, the DTA thermogram of RGO–CS (dashed line) shows a small exothermic peak in this region centered at 280 °C, which is in good agreement with the thermal decomposition temperature reported for starch [111]. Then, we can argue that the starch-like phase accounts for about 8% of the mass of RGO–CS 10%. Therefore, notwithstanding the changes that both GO and CS have experienced, the CS* content in the reduced hybrid samples turns out to be relatively close to the chitosan content initially added to GO. By further increase of the temperature, RGO shows a single combustion peak centered at 622 °C, whereas RGO–CS appears to have a peak at 610 °C with a shoulder at 622 °C. From this, we infer that RGO surface regions decorated with the starch-like phase may have a slightly modified thermal stability, causing a bimodal burning behavior of the hybrid.

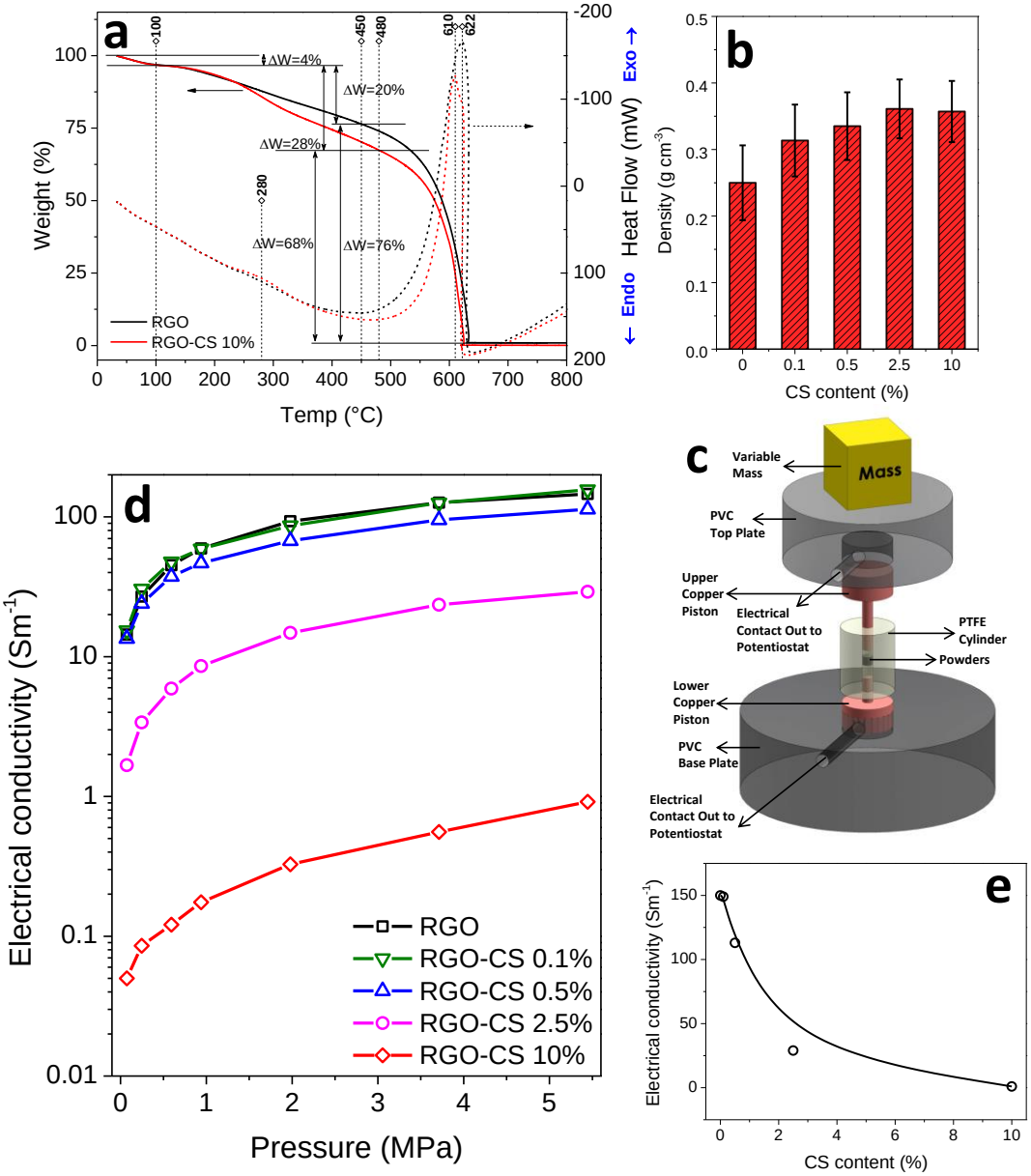

Fig. 5. (a) TGA (solid lines, left axis) and DTA (dashed lines, right axis) curves of RGO and RGO–CS 10%, (b) packing density of the free standing hybrid pastes *vs.* CS content, (c) schematic of the cell used for the electrical conductivity measurements [20], (d) electrical conductivity of compacted powder samples and (e) highest measured conductivity of samples *vs.* CS content.

Fig. 5b shows the apparent density of the samples. For two-dimensional electrode materials, like RGO, the non-compact nature of sheet arrangement limits their volumetric energy density, unless a packing strategy is implemented allowing for closer settlement of the sheets without substantial loss of surface area. Therefore, a high packing density is essential in order to achieve a relatively high volumetric energy density [110]. The packing density measurement were performed on self-standing sheets, fabricated using the same procedure as for the electrodes, not on the powder, since the bulk density of powders is

dependent on the degree of compaction. We thought more significant to test the materials in the same state as the freestanding electrodes, in view of the expected relevance of this property to the electrochemical behavior of the hybrids. Since graphene is a soft and loose material, packing densities as low as 0.05 g cm^{-3} have been reported for such electrodes in the uncompressed state [112]. Whereas packing density in the range 0.2-0.45 g cm^{-3} is typical of uncompressed electrodes made by rolling a paste [113–116], higher density, in the range 0.7 to 1.33 g cm^{-3}, is reported using different compaction methods such as hydraulic pressing [114,117] or capillary compression [118]. The packing density of our electrodes varies between 0.25 g cm^{-3} for RGO to 0.36 g cm^{-3} for RGO–CS 2.5%, see Fig. 5b. According to the model reported in [118], the above increase in the density corresponds to a decrease in the average inter-sheet spacing of graphene layers from ~ 4.25 nm for RGO to ~ 3 nm for RGO–CS 2.5%. Apparently, the CS hybridization can increase the packing of the RGO layers (by almost 44%) and decrease their spacing (by almost 30%). From these results, we infer that the reactive attachment of CS molecules onto RGO sheets has the effect of a stiffener, decreasing creases, wrinkles and folding of RGO, and, in turn, increasing the packing density, since a higher number of individual RGO sheets bundle up per unit volume. An alternative, or complementary, explanation for the higher packing of the hybrids is that CS^{*} modifies RGO sheets to acquire anti-adhesive properties, thus preventing, to a certain extent, re-stacking and agglomeration. In RGO sample, relatively large agglomerates are formed (Fig. 1a), which inevitably develop large macropores in between and contribute to a loose packing. Since, as shown in Fig. 5b, the packing density of the electrodes appears to level off for CS content beyond the RGO–CS 2.5% level, we presume that the limiting inter-sheet spacing for relatively flattened graphene layers is reached at CS content of 2.5%, so that further packing is not possible. Further discussion of these results will follow in section 3.5.2.

The electrical conductivity is another physical property that was characterized, using the lab-made set-up shown in the schematic of Fig. 5c. Similar to the packing density, the electrical conductivity shows a clear and strong dependence on the CS content, as shown in Fig. 5d for different samples. The conductivity increases by the compaction pressure because of improved inter-particle contact, revealing a limiting value at high enough pressure. Conductivity values corresponding to the high-end pressure are plotted in Fig. 5e as a function of the CS content of hybrids. The conductivity of the pure RGO compacted powder

is about 150 S m^{-1}, which is remarkably high. At small CS content (e.g., 0.1%), the conductivity remains unchanged, while it decreases for CS content beyond 0.5%.

3.5 Electrochemical characterization

As a complement and completion of the physical-chemical investigation of the hybrids, we performed an electrochemical study of the capacitive performance of RGO–CS hybrid based electrodes, in consideration of the widespread use of RGO varieties for this particular application [119–121]. RGO and RGO–CS electrodes were characterized by CV for assessing the capacitive performance metrics and EIS for evaluating the underlying charge storage mechanism. Testing was performed in a three-electrode configuration only, since the main objective of this study was the electrode material behavior.

3.5.1 Cyclic voltammetry

Fig. 6 shows the CV results for RGO–CS electrodes as gravimetric, C_g, (a, b, c) and volumetric, C_v, (d, e, f) capacitance *vs.* potential. Voltammograms at the lowest scan rate (1 mV s^{-1}, Fig. 6a and d) reveal the capacitive nature of the interface by the semi-rectangular shape of the curve, though a gradual rise of the current at the positive end of the potential range is evident, due supposedly to the oxidation of surface functionalities of carbon [122]. In addition, large symmetric humps appear at about 0.3 V, a feature that can be attributed to the redox conversion of quinone-hydroquinone groups [123]. The CS content affects both the gravimetric and volumetric capacitance, but the extent of the effect is larger with the latter. Fig. 6b and e show the change of C_g and C_v, respectively, with the scan rate, for a comparative assessment of the rate capability of the electrodes. In this respect, RGO–CS 0.1% and RGO–CS 0.5% reveal a similar behavior as RGO; RGO–CS 2.5% shows lower rate sensitivity compared to RGO, and notably the best rate capability in terms of C_g ; RGO–CS 10%, with the highest CS content, shows the highest loss of C_g and C_v with the scan rate. Summing up, with regard to the effect of CS content on specific capacitance, either gravimetric (C_g) or volumetric (C_v), RGO–CS 0.5% is the optimum composition over the given scan rate range (Fig. 6c and f), though RGO–CS 2.5% appears to reach comparable performance at the high end of the scan rate range, particularly in terms of C_v.

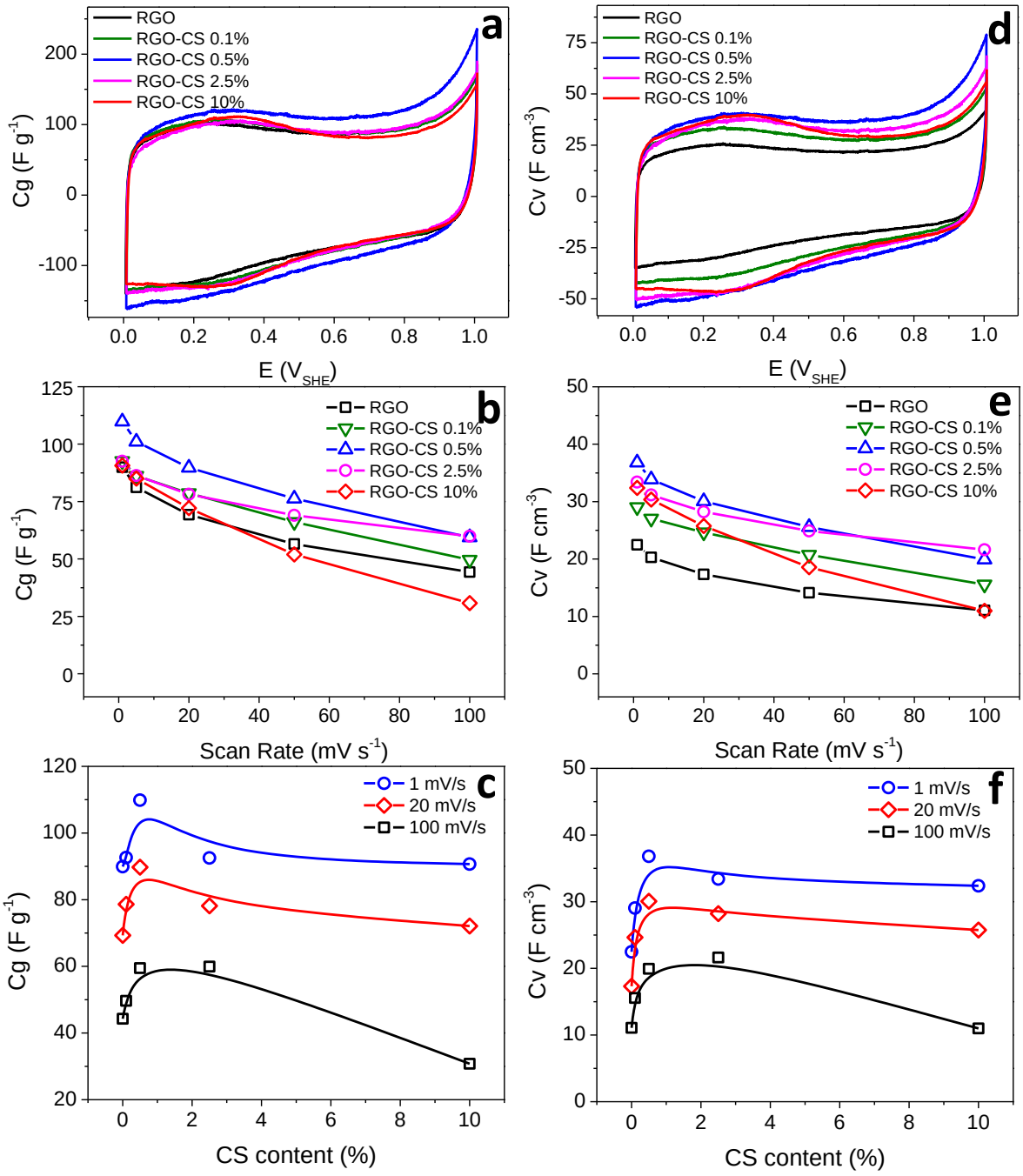

Fig. 6 Results of the electrochemical characterization of the hybrid samples with different CS content by CV in 1 M Na_2SO_4 electrolyte, at the scan rate of 1 mV s^{-1}; (a) gravimetric and (d) volumetric capacitance *vs.* potential, (b and e) C_g and C_v, respectively, *vs.* scan rate and (c and f) C_g and C_v, respectively, *vs.* CS content, at three typical scan rates. Solid lines in (b, e) and (c, f) are drawn as a guide to the eye.

Interestingly, the volumetric capacitance is the quantity revealing the strongest sensitivity to RGO modification by CS. Specifically, the RGO volumetric capacitance C_v improves upon hybrid formation with CS (at the optimum composition) by 64% at 1 mV s^{-1} and by 92% at 100 mV s^{-1}, compared to the 22–35% increase of the gravimetric capacitance C_g under the same conditions. These differences in the

extent of the change of C_g and C_v in the hybrid must have their origin in the mechanism through which the charge storage capability of RGO is modified by CS. We hypothesize that two closely related yet distinct factors are contributing to these effects. Firstly, CS acts as a barrier against adhesion between RGO sheets, thereby reducing the van der Waals driven re-stacking, and this process affects equally C_g and C_v. Secondly, the attachment of CS molecules onto RGO sheets produces a stiffening effect, thus reducing creasing and increasing packing density as discussed earlier (Fig. 5b). We believe this second phenomenon affects chiefly the volumetric capacitance. The notion of exploiting the stiffening effect of starch has a long tradition in the textile [124] and in the pulp and paper industries [125]. However, the exploitation of this phenomenon for nanoscale flexible 2D materials, such as RGO, has not yet emerged. For a more in depth assessment of the above hypotheses, we performed EIS analysis of the electrodes, as discussed in the next section.

3.5.2 Electrochemical impedance spectroscopy

The plots in Fig. 7 outline the results of the EIS analysis. The Nyquist plots of the spectra are compared in Fig. 7a and shown individually in Fig. 7c-g together with fitting results to the equivalent circuit shown in Fig. 7b. In this model, R_{esr} is the equivalent series resistance accounting for the sum of the electrolyte resistance and the ohmic resistance of the electrode materials. C_{cont} and R_{cont}, are the contact capacitance and resistance, respectively, at the active material and the graphite current collector interface. C_{cap} represents the capacitive contribution of the porous electrode by double layer charging. Both C_{cont} and C_{cap} were modeled using constant phase elements (CPE). W represents the diffusion impedance, modeled using the finite-length Warburg element for reflective boundary, i.e. Warburg open (W_O) element [126]. The equivalent circuit model was chosen based on several reasons, after comparison with many other models: physical significance in describing the behavior of the material under study, mathematical fit to the experimental data with minimum error, and relative simplicity. Some components used routinely in other models, such as the charge transfer resistance, or a double-branched capacitive feature accounting for both double layer- and pseudo-capacitive contributions, were found inessential. The satisfactory quality of the fit can be seen in Fig. 7c-g for different electrodes, and the variation of the equivalent circuit components with the CS content is shown in Fig. 7h-l. R_{esr} (Fig. 7h) increases slightly

with the CS content, mainly due to the electrode material resistance, in agreement with electrical conductivity data (Fig. 5 d and e). More interesting is that the contact resistance, R_{cont} (Fig. 7i), increases dramatically with the CS content, its relative increase being almost 5 times larger than the corresponding change of R_{esr}. The capacitive component at the active material/graphite interface, C_{cont}, which is normalized to the geometrical area in Fig. 7j, is about 2.5 mF cm^{-2} and changes only slightly with the CS content, except for RGO–CS 10%. It is important to note that the CPE exponent (CPE_{P-cont} in the inset of Fig. 7j) drops gradually with the CS content revealing a resistive shift in the behavior, so that the presumption of C_{cont} being a capacitance is no longer acceptable for RGO–CS 10%. Fig. 7k and l, show the components of the W_O element. The diffusion impedance of W_O is expressed as [126,127]:

$$Z_{W_O} = \frac{W_R}{(jW_T\omega)^p}\coth[(jW_T\omega)^p] \quad (4)$$

where W_R (Ω) is the Warburg resistance [128,129], $W_T = \frac{\delta^2}{D}$ (s), is the characteristic diffusion time constant, representing the ratio of the square of the effective diffusion length δ to the diffusion coefficient D, and p is the exponent in the range $0 \leq p \leq 1$, with the ideal case of finite space behavior characterized by $p = 1/2$.

Warburg resistance, W_R, is a function of the temperature, of the diffusion coefficient of the ionic species, of their concentration in the bulk electrolyte and in the pores of the electrode, and of the electrochemically active surface area [130]. Therefore, under the fixed conditions of temperature and electrolyte bulk concentration of our experiments, this parameter reflects the influence of the textural properties of the porous electrode on ionic transport. This parameter follows a similar trend as the main capacitive component, C_{cap} (normalized to the electrode active mass, C_g, in Fig. 7m).

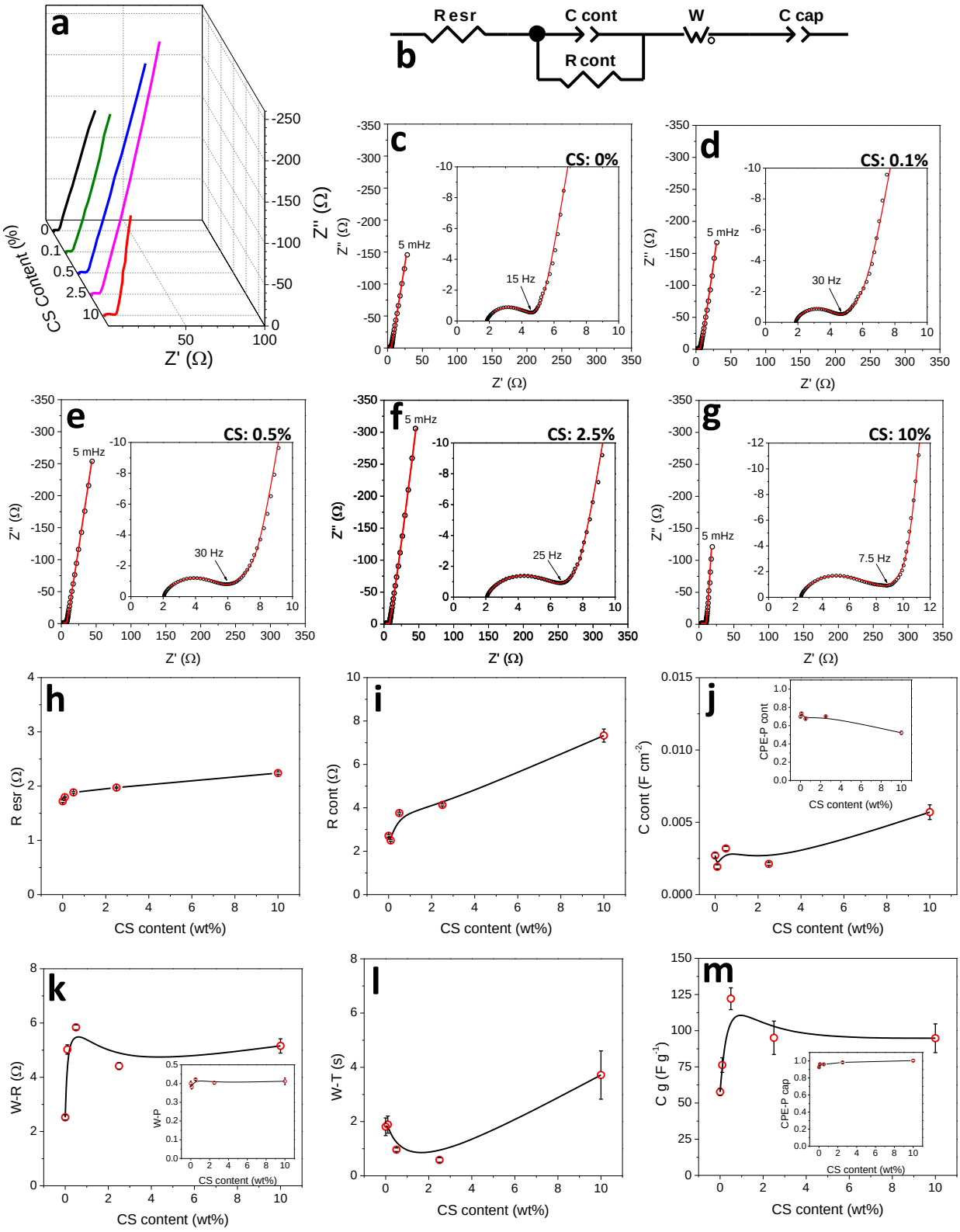

Fig. 7 (a) Nyquist plots of RGO and RGO–CS electrodes; (b) equivalent circuit used to model the EIS spectra; (c–g) fitting results of the model (solid lines) to the experimental data (symbols) for all electrodes as indicated; and (h–m) change of the equivalent circuit components *vs.* CS content: (h) R_{esr}, (i) R_{cont}, (j) C_{cont} (this element was modeled using a CPE with the exponent CPE_{P-cont} shown in the inset), (k) W_R (with the exponent W_P shown in the inset), (l) W_T, and finally, (m) the main capacitive component of the circuit, C_{cap}, normalized to the electrode active mass to represent C_g (this element was modeled using a CPE with the exponent CPE_{P-cap} shown in the inset). Lines in plots (h) to (m) are drawn as a guide to the eye.

Therefore, we infer that the modification of the porous structure associated with the RGO–CS hybrid formation has a two-fold effect: namely, a relative increase of the specific capacitance, on the one hand, and of the diffusion resistance, on the other hand. Given the strong increase of specific capacitance, this diverging influence does not conflict with the changes of W_T, which confirms fastest electrode response to the potential perturbation at the composition showing the best rate performance in CV experiments, namely, RGO–CS 2.5%. Surprisingly, the sample with the highest packing density (Fig. 5b) allows fastest ion diffusion (with W_T=0.585 s compared to 1.80 s for RGO).

For the assessment of the relaxation time, τ_0, the imaginary component of the complex capacitance was calculated from the EIS data according to the following equation [131]:

$$C''(\omega) = \frac{Z'(\omega)}{\omega |Z(\omega)|^2} \qquad (5)$$

where $C''(\omega)$ is the imaginary component of the complex capacitance $C(\omega)$, $Z'(\omega)$ is the real component of the complex impedance $Z(\omega)$, $|Z(\omega)|$ is the magnitude of impedance and ω is the angular frequency. The relaxation frequency (f_0), at which the behavior of the electrode shifts from predominantly resistive to capacitive, is revealed as a peak on the imaginary capacitance curve (Fig. 8a, $C''(f)$). The relaxation time can be calculated on this basis as the reciprocal of f_0, and compared for different electrodes (Fig. 8b). Since τ_0 corresponds to a compromise between the global resistance (including all resistive features such as electric and contact resistance of the active material, electrolyte resistance, ionic resistance in pores due to diffusion, charge transfer resistance of parasitic reactions, etc.) and the global capacitance, larger values are observed in comparison with W_T. Nevertheless, the trend of change is the same for both and the optimum rate performance of RGO–CS 2.5% is confirmed.

According to the interpretation of the impedance response and the analysis of the packing density, we conclude that the densification process driven by CS, as discussed earlier, rather than leading to sheet re-stacking and pore blocking – as it could be expected – has a beneficial effect on ion diffusion, arguably by modifications of the electrode pore structure such as enhancement of pore connectivity and widening of ion diffusion channels. We sought independent confirmation of this inference through the textural study of the RGO–CS 2.5% sample in comparison with the pure RGO. The BJH pore size distribution in

Fig. 8c reveals that both materials are dominantly of mesoporous nature with a most probable pore size in the range of 3.5 nm. In fact, the introduction of CS does not change drastically the innate distribution of the pore size in RGO, but rather increases the relative contribution of the small size mesopore fraction at the expense of the large size mesopore and macropore content. This is revealed clearly in the plot of Fig. 8c by the shifting up of the pore size distribution peak and the sinking of the distribution curve in the range of 10 to 30 nm pore size.

The evaluation of the SSA by the BET method shows that the formation of the hybrid causes almost a doubling of the available surface for N_2 adsorption. However, the absolute values of the obtained figures (26.85 and 58.43 m^2g^{-1} for RGO and RGO–CS 2.5%, respectively) should be considered with caution. Based on the theoretical calculations of Peigney et al. [10], who proposed an SSA of 1315 m^2g^{-1} for the external surface of single-walled carbon nanotubes, theoretical SSA values up to 2630 m^2g^{-1} have been attributed to single layer graphene [4,5]. Nonetheless, SSA values derived from BET analysis of chemically reduced graphene oxide are considerably lower, ranging from 5 m^2g^{-1} [132] to 600 m^2g^{-1} [133,134], with a remarkable frequency between 50–250 m^2g^{-1} [135–137].

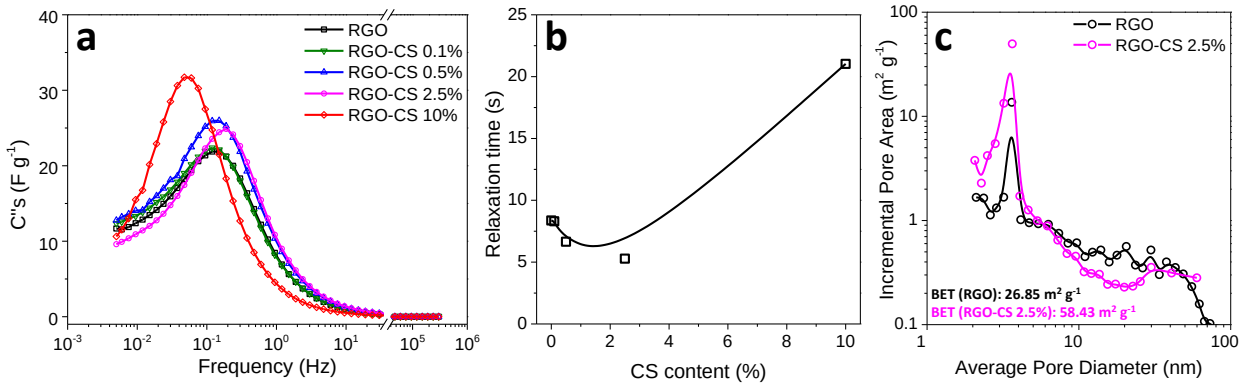

Fig. 8 (a) The imaginary component of the complex capacitance $C''(f)$ *vs.* frequency for different samples, (b) relaxation time, τ_0, *vs.* CS content and (c) the BJH pore size distribution (pore area vs. pore diameter) of RGO and RGO–CS 2.5%.

Such apparently low values of SSA for RGO materials have been attributed to either incomplete exfoliation of GO sheets during graphite oxidation, or to re-stacking of RGO sheets and self-aggregation upon drying. Nevertheless, the capabilities of the SSA probing technique should also be taken into account. According to Guo et al. [138] as well as Xu et al. [117], moving from BET (even though RGO

samples were freeze-dried to minimize re-stacking during drying) to methylene blue adsorption method in a liquid medium, the SSA increased by a factor of up to four. In addition to the re-stacking issue, possibly limiting access of N_2 to the surface, another source of uncertainty in the SSA predicted by BET may be the high permanent quadrupole moment of N_2 [139] which can promote specific interactions with surface functional groups [140] of RGO leading to clogging of microporous channels.

An alternative way to evaluate the SSA is to use the specific capacitance, C_g (F g^{-1}), observed at low rate to ensure ion access to the entire electrochemical surface area, and the areal capacitance, C_a (F cm^{-2}), of carbon materials. We determined the gravimetric capacitance of the electrodes by CV (Fig. 6) and EIS (Fig. 7m), finding complete agreement between the two methods, in terms of both the trend with CS content, and the range of values. The literature reports values of the double layer capacitance of carbon [141] in the range from 5 to 20 μF cm^{-2}, though values larger than 10 μF cm^{-2} are usually explained in terms of a pseudocapacitive contribution to interface charging. Assuming a dominant double layer charging mechanism for the electrodes and a C_a value of 10 μF cm^{-2}, using the C_g values for different samples (averaged from CV and EIS), we obtain for the electrochemically accessible surface area values of 738, 844, 1160, 938 and 927 m^2g^{-1} for samples RGO, RGO–CS 0.1%, RGO–CS 0.5%, RGO–CS 2.5% and RGO–CS 10%, respectively. Even considering a high pseudocapacitance contribution, and thus using a high-end C_a value of 20 μF cm^{-2}, the obtained SSA values (369, 422, 580, 469 and 463.5 m^2g^{-1} for samples RGO, RGO–CS 0.1%, RGO–CS 0.5%, RGO–CS 2.5% and RGO–CS 10%, respectively) remain far larger than the BET based evaluation.

4 Conclusion

In this work, we describe the formation of a reduced graphene oxide / chitosan hybrid via chemical reduction of a graphene oxide – chitosan precursor. In the concentration range of CS studied in this work (0.1–10 wt%), physical properties, such as packing density, electrical conductivity and BET surface area were remarkably changed with respect to single phase RGO. A rigorous and critical examination of XRD and ATR-FTIR results revealed characteristic similarities between the CS modification in the RGO–CS hybrid and polysaccharides, such as cellulose and starch. Precisely, we found that A-type starch shows a meaningful match with most crystallographic and spectroscopic features observed in the hybrid and

lacking in the RGO. Our conclusion is that a pseudo-starch phase forms in the course of the thermochemical reduction through simultaneous partial deoxygenation and deacetylation of hydrolyzed chitosan fragments attached onto GO sheets. Noteworthily, based on TGA, we estimate that the CS derivative content in the hybrids is not far from the chitosan content initially added to the original GO–CS mixture. The characterization of the electrochemical capacitive behavior of RGO–CS hybrids provides further evidence in support of the above conclusions. The gravimetric and volumetric capacitance (C_g and C_v, respectively) were improved at the optimum CS content by up to 35% and 92%, respectively, compared to pure RGO. The RGO–CS 2.5% hybrid revealed the largest extent of modification among hybrid samples, with 44% percent increase in the packing density and an evident increase in the specific surface area due to enhancement of the small size pore fraction in the mesoporous region. The main possible drawback of the formation of RGO–CS hybrids is the lower conductivity compared to RGO. However, the RGO–CS 2.5% shows not only the best capacitive performance, but also the best rate performance. The fact that the densest sample (RGO–CS 2.5%, ρ=0.36 g cm^{-3}), showed the fastest frequency response, demonstrates that the densification process driven by CS, rather than leading to sheet re-stacking and pore blocking, has a beneficial effect on ion diffusion, in agreement with the pore texture modification.

In conclusion, we explain the properties of RGO–CS hybrids based on a two-fold effect: first, the surface decoration of RGO sheets by the CS derived phase acts as a barrier against re-staking of RGO sheets; secondly, the reactive attachment of CS molecules onto RGO sheets produces a stiffening effect, mitigating their crumpling, and allowing a denser packing.

This research did not receive any specific grant from funding agencies in the public, commercial, or not-for-profit sectors.

References

[1] W. Choi, I. Lahiri, R. Seelaboyina, Y.S. Kang, Synthesis of Graphene and Its Applications: A Review, Critical Reviews in Solid State and Materials Sciences. 35 (2010) 52–71. https://doi.org/10.1080/10408430903505036.

[2] K.S. Novoselov, A.K. Geim, S.V. Morozov, D. Jiang, Y. Zhang, S.V. Dubonos, I.V. Grigorieva, A.A. Firsov, Electric Field Effect in Atomically Thin Carbon Films, Science. 306 (2004) 666–669. https://doi.org/10.1126/science.1102896.
[3] D.S.L. Abergel, V. Apalkov, J. Berashevich, K. Ziegler, T. Chakraborty, Properties of graphene: a theoretical perspective, Advances in Physics. 59 (2010) 261–482. https://doi.org/10.1080/00018732.2010.487978.
[4] S. Guo, S. Dong, Graphene nanosheet: synthesis, molecular engineering, thin film, hybrids, and energy and analytical applications, Chem. Soc. Rev. 40 (2011) 2644. https://doi.org/10.1039/c0cs00079e.
[5] F. Bonaccorso, L. Colombo, G. Yu, M. Stoller, V. Tozzini, A.C. Ferrari, R.S. Ruoff, V. Pellegrini, Graphene, related two-dimensional crystals, and hybrid systems for energy conversion and storage, Science. 347 (2015) 1246501. https://doi.org/10.1126/science.1246501.
[6] W.S. Hummers, R.E. Offeman, Preparation of Graphitic Oxide, J. Am. Chem. Soc. 80 (1958) 1339–1339. https://doi.org/10.1021/ja01539a017.
[7] N.I. Kovtyukhova, P.J. Ollivier, B.R. Martin, T.E. Mallouk, S.A. Chizhik, E.V. Buzaneva, A.D. Gorchinskiy, Layer-by-Layer Assembly of Ultrathin Composite Films from Micron-Sized Graphite Oxide Sheets and Polycations, Chem. Mater. 11 (1999) 771–778. https://doi.org/10.1021/cm981085u.
[8] C.K. Chua, M. Pumera, Chemical reduction of graphene oxide: a synthetic chemistry viewpoint, Chem. Soc. Rev. 43 (2014) 291–312. https://doi.org/10.1039/C3CS60303B.
[9] D.R. Dreyer, S. Park, C.W. Bielawski, R.S. Ruoff, The chemistry of graphene oxide, Chem. Soc. Rev. 39 (2010) 228–240. https://doi.org/10.1039/B917103G.
[10] A. Peigney, Ch. Laurent, E. Flahaut, R.R. Bacsa, A. Rousset, Specific surface area of carbon nanotubes and bundles of carbon nanotubes, Carbon. 39 (2001) 507–514. https://doi.org/10.1016/S0008-6223(00)00155-X.
[11] S. Pei, H.-M. Cheng, The reduction of graphene oxide, Carbon. 50 (2012) 3210–3228. https://doi.org/10.1016/j.carbon.2011.11.010.
[12] S. Stankovich, D.A. Dikin, R.D. Piner, K.A. Kohlhaas, A. Kleinhammes, Y. Jia, Y. Wu, S.T. Nguyen, R.S. Ruoff, Synthesis of graphene-based nanosheets via chemical reduction of exfoliated graphite oxide, Carbon. 45 (2007) 1558–1565. https://doi.org/10.1016/j.carbon.2007.02.034.
[13] J. Zhang, H. Yang, G. Shen, P. Cheng, J. Zhang, S. Guo, Reduction of graphene oxide via L -ascorbic acid, Chem. Commun. 46 (2010) 1112–1114. https://doi.org/10.1039/B917705A.
[14] M.J. Fernández-Merino, L. Guardia, J.I. Paredes, S. Villar-Rodil, P. Solís-Fernández, A. Martínez-Alonso, J.M.D. Tascón, Vitamin C Is an Ideal Substitute for Hydrazine in the Reduction of Graphene Oxide Suspensions, J. Phys. Chem. C. 114 (2010) 6426–6432. https://doi.org/10.1021/jp100603h.
[15] C. Li, X. Zhang, K. Wang, H. Zhang, X. Sun, Y. Ma, Three dimensional graphene networks for supercapacitor electrode materials, New Carbon Materials. 30 (2015) 193–206. https://doi.org/10.1016/S1872-5805(15)60185-8.
[16] Y. Xu, K. Sheng, C. Li, G. Shi, Self-Assembled Graphene Hydrogel via a One-Step Hydrothermal Process, ACS Nano. 4 (2010) 4324–4330. https://doi.org/10.1021/nn101187z.
[17] K. Sheng, Y. Xu, C. Li, G. Shi, High-performance self-assembled graphene hydrogels prepared by chemical reduction of graphene oxide, New Carbon Materials. 26 (2011) 9–15. https://doi.org/10.1016/S1872-5805(11)60062-0.
[18] Q. Cheng, J. Tang, J. Ma, H. Zhang, N. Shinya, L.-C. Qin, Graphene and carbon nanotube composite electrodes for supercapacitors with ultra-high energy density, Physical Chemistry Chemical Physics. 13 (2011) 17615. https://doi.org/10.1039/c1cp21910c.
[19] C. Zheng, X. Zhou, H. Cao, G. Wang, Z. Liu, Synthesis of porous graphene/activated carbon composite with high packing density and large specific surface area for supercapacitor electrode material, Journal of Power Sources. 258 (2014) 290–296. https://doi.org/10.1016/j.jpowsour.2014.01.056.
[20] M. Hashempour, A. Vicenzo, M. Bahdanchyk, M. Bestetti, Parameters influencing the capacitive behavior of carbon composite electrodes: composition, morphology, electrical conductivity, and surface chemistry, J Solid State Electrochem. 22 (2018) 3895–3911. https://doi.org/10.1007/s10008-018-4095-8.

[21] Y. Si, E.T. Samulski, Exfoliated Graphene Separated by Platinum Nanoparticles, Chem. Mater. 20 (2008) 6792–6797. https://doi.org/10.1021/cm801356a.
[22] T. Li, N. Li, J. Liu, K. Cai, M.F. Foda, X. Lei, H. Han, Synthesis of functionalized 3D porous graphene using both ionic liquid and SiO_2 spheres as "spacers" for high-performance application in supercapacitors, Nanoscale. 7 (2015) 659–669. https://doi.org/10.1039/C4NR05473C.
[23] J.H. Lee, N. Park, B.G. Kim, D.S. Jung, K. Im, J. Hur, J.W. Choi, Restacking-Inhibited 3D Reduced Graphene Oxide for High Performance Supercapacitor Electrodes, ACS Nano. 7 (2013) 9366–9374. https://doi.org/10.1021/nn4040734.
[24] M.M. Sk, C.Y. Yue, Layer-by-layer (LBL) assembly of graphene with p-phenylenediamine (PPD) spacer for high performance supercapacitor applications, RSC Adv. 4 (2014) 19908. https://doi.org/10.1039/c4ra02652g.
[25] M.N.V. Ravi Kumar, A review of chitin and chitosan applications, Reactive and Functional Polymers. 46 (2000) 1–27. https://doi.org/10.1016/S1381-5148(00)00038-9.
[26] C.K.S. Pillai, W. Paul, C.P. Sharma, Chitin and chitosan polymers: Chemistry, solubility and fiber formation, Progress in Polymer Science. 34 (2009) 641–678. https://doi.org/10.1016/j.progpolymsci.2009.04.001.
[27] J. Lizardi-Mendoza, W.M. Argüelles Monal, F.M. Goycoolea Valencia, Chemical Characteristics and Functional Properties of Chitosan, in: Chitosan in the Preservation of Agricultural Commodities, Elsevier, 2016: pp. 3–31. https://doi.org/10.1016/B978-0-12-802735-6.00001-X.
[28] Annu, A.N. Raja, Recent development in chitosan-based electrochemical sensors and its sensing application, International Journal of Biological Macromolecules. 164 (2020) 4231–4244. https://doi.org/10.1016/j.ijbiomac.2020.09.012.
[29] X. He, P. Song, X. Shen, Y. Sun, Z. Ji, H. Zhou, B. Li, Chitosan-assisted synthesis of wearable textile electrodes for high-performance electrochemical energy storage, Cellulose. 26 (2019) 9349–9359. https://doi.org/10.1007/s10570-019-02727-z.
[30] B.K. Roy, I. Tahmid, T.U. Rashid, Chitosan-based materials for supercapacitor applications: a review, J. Mater. Chem. A. (2021) 10.1039.D1TA02997E. https://doi.org/10.1039/D1TA02997E.
[31] R. Vinodh, Y. Sasikumar, H.-J. Kim, R. Atchudan, M. Yi, Chitin and chitosan based biopolymer derived electrode materials for supercapacitor applications: A critical review, Journal of Industrial and Engineering Chemistry. 104 (2021) 155–171. https://doi.org/10.1016/j.jiec.2021.08.019.
[32] L. Sun, Y. Fu, C. Tian, Y. Yang, L. Wang, J. Yin, J. Ma, R. Wang, H. Fu, Isolated Boron and Nitrogen Sites on Porous Graphitic Carbon Synthesized from Nitrogen-Containing Chitosan for Supercapacitors, ChemSusChem. 7 (2014) 1637–1646. https://doi.org/10.1002/cssc.201400048.
[33] Z. Ling, G. Wang, M. Zhang, X. Fan, C. Yu, J. Yang, N. Xiao, J. Qiu, Boric acid-mediated B,N-codoped chitosan-derived porous carbons with a high surface area and greatly improved supercapacitor performance, Nanoscale. 7 (2015) 5120–5125. https://doi.org/10.1039/C5NR00081E.
[34] P. Hao, Z. Zhao, Y. Leng, J. Tian, Y. Sang, R.I. Boughton, C.P. Wong, H. Liu, B. Yang, Graphene-based nitrogen self-doped hierarchical porous carbon aerogels derived from chitosan for high performance supercapacitors, Nano Energy. 15 (2015) 9–23. https://doi.org/10.1016/j.nanoen.2015.02.035.
[35] A. Śliwak, N. Díez, E. Miniach, G. Gryglewicz, Nitrogen-containing chitosan-based carbon as an electrode material for high-performance supercapacitors, J Appl Electrochem. 46 (2016) 667–677. https://doi.org/10.1007/s10800-016-0955-z.
[36] L. Zhu, F. Shen, R.L. Smith, X. Qi, High-Performance Supercapacitor Electrode Materials from Chitosan via Hydrothermal Carbonization and Potassium Hydroxide Activation, Energy Technol. 5 (2017) 452–460. https://doi.org/10.1002/ente.201600337.
[37] B. Li, Y. Cheng, L. Dong, Y. Wang, J. Chen, C. Huang, D. Wei, Y. Feng, D. Jia, Y. Zhou, Nitrogen doped and hierarchically porous carbons derived from chitosan hydrogel via rapid microwave carbonization for high-performance supercapacitors, Carbon. 122 (2017) 592–603. https://doi.org/10.1016/j.carbon.2017.07.009.
[38] Z. Li, L. Yang, H. Cao, Y. Chang, K. Tang, Z. Cao, J. Chang, Y. Cao, W. Wang, M. Gao, C. Liu, D. Liu, H. Zhao, Y. Zhang, M. Li, Carbon materials derived from chitosan/cellulose cryogel-supported zeolite imidazole frameworks for potential supercapacitor application, Carbohydrate Polymers. 175 (2017) 223–230. https://doi.org/10.1016/j.carbpol.2017.07.089.

[39] M. Genovese, H. Wu, A. Virya, J. Li, P. Shen, K. Lian, Ultrathin all-solid-state supercapacitor devices based on chitosan activated carbon electrodes and polymer electrolytes, Electrochimica Acta. 273 (2018) 392–401. https://doi.org/10.1016/j.electacta.2018.04.061.
[40] L. Yang, D. Wu, T. Wang, D. Jia, B/N-Codoped Carbon Nanosheets Derived from the Self-Assembly of Chitosan–Amino Acid Gels for Greatly Improved Supercapacitor Performances, ACS Appl. Mater. Interfaces. 12 (2020) 18692–18704. https://doi.org/10.1021/acsami.0c01655.
[41] X. Tong, Z. Chen, H. Zhuo, Y. Hu, S. Jing, J. Liu, L. Zhong, Tailoring the physicochemical properties of chitosan-derived N-doped carbon by controlling hydrothermal carbonization time for high-performance supercapacitor application, Carbohydrate Polymers. 207 (2019) 764–774. https://doi.org/10.1016/j.carbpol.2018.12.048.
[42] M. Yuan, Y. Zhang, B. Niu, F. Jiang, X. Yang, M. Li, Chitosan-derived hybrid porous carbon with the novel tangerine pith-like surface as supercapacitor electrode, J Mater Sci. 54 (2019) 14456–14468. https://doi.org/10.1007/s10853-019-03911-z.
[43] G. Sun, B. Li, J. Ran, X. Shen, H. Tong, Three-dimensional hierarchical porous carbon/graphene composites derived from graphene oxide-chitosan hydrogels for high performance supercapacitors, Electrochimica Acta. 171 (2015) 13–22. https://doi.org/10.1016/j.electacta.2015.05.009.
[44] Y. Zhang, J.-Y. Zhu, H.-B. Ren, Y.-T. Bi, L. Zhang, Facile synthesis of nitrogen-doped graphene aerogels functionalized with chitosan for supercapacitors with excellent electrochemical performance, Chinese Chemical Letters. 28 (2017) 935–942. https://doi.org/10.1016/j.cclet.2017.01.023.
[45] M. Gao, L. Wang, B. Zhao, X. Gu, T. Li, L. Huang, Q. Wu, S. Yu, S. Liu, Sandwich construction of chitosan/reduced graphene oxide composite as additive-free electrode material for high-performance supercapacitors, Carbohydrate Polymers. 255 (2021) 117397. https://doi.org/10.1016/j.carbpol.2020.117397.
[46] M.G. Hosseini, E. Shahryari, A Novel High-Performance Supercapacitor based on Chitosan/Graphene Oxide-MWCNT/Polyaniline, Journal of Colloid and Interface Science. 496 (2017) 371–381. https://doi.org/10.1016/j.jcis.2017.02.027.
[47] K.Z. Htut, M. Kim, E. Lee, G. Lee, S.H. Baeck, S.E. Shim, Biodegradable polymer-modified graphene/polyaniline electrodes for supercapacitors, Synthetic Metals. 227 (2017) 61–70. https://doi.org/10.1016/j.synthmet.2017.03.005.
[48] A. Gopalakrishnan, N. Vishnu, S. Badhulika, Cuprous oxide nanocubes decorated reduced graphene oxide nanosheets embedded in chitosan matrix: A versatile electrode material for stable supercapacitor and sensing applications, Journal of Electroanalytical Chemistry. 834 (2019) 187–195. https://doi.org/10.1016/j.jelechem.2018.12.051.
[49] N.R. Aswathy, A.K. Palai, A. Ramadoss, S. Mohanty, S.K. Nayak, Fabrication of cellulose acetate-chitosan based flexible 3D scaffold-like porous membrane for supercapacitor applications with PVA gel electrolyte, Cellulose. 27 (2020) 3871–3887. https://doi.org/10.1007/s10570-020-03030-y.
[50] E.S. Al-Farraj, A.N. Alhabarah, J. Ahmad, A.M. Al-Enizi, M. Naushad, M. Ubaidullah, S.M. Alshehri, Ruksana, T. Ahamad, Fabrication of hybrid nanocomposite derived from chitosan as efficient electrode materials for supercapacitor, International Journal of Biological Macromolecules. 120 (2018) 2271–2278. https://doi.org/10.1016/j.ijbiomac.2018.08.104.
[51] R.B. Suneetha, P. Selvi, C. Vedhi, Synthesis, structural and electrochemical characterization of Zn doped iron oxide/grapheneoxide/chitosan nanocomposite for supercapacitor application, Vacuum. 164 (2019) 396–404. https://doi.org/10.1016/j.vacuum.2019.03.051.
[52] D. Han, T. Han, C. Shan, A. Ivaska, L. Niu, Simultaneous Determination of Ascorbic Acid, Dopamine and Uric Acid with Chitosan-Graphene Modified Electrode, Electroanalysis. 22 (2010) 2001–2008. https://doi.org/10.1002/elan.201000094.
[53] J.-S. Cheng, J. Du, W. Zhu, Facile synthesis of three-dimensional chitosan–graphene mesostructures for reactive black 5 removal, Carbohydrate Polymers. 88 (2012) 61–67. https://doi.org/10.1016/j.carbpol.2011.11.065.
[54] T. Jiao, H. Zhao, J. Zhou, Q. Zhang, X. Luo, J. Hu, Q. Peng, X. Yan, Self-Assembly Reduced Graphene Oxide Nanosheet Hydrogel Fabrication by Anchorage of Chitosan/Silver and Its Potential Efficient Application toward Dye Degradation for Wastewater Treatments, ACS Sustainable Chemistry & Engineering. 3 (2015) 3130–3139. https://doi.org/10.1021/acssuschemeng.5b00695.

[55] N.A. Salleh, S. Kheawhom, A.A. Mohamad, Chitosan as biopolymer binder for graphene in supercapacitor electrode, Results in Physics. 25 (2021) 104244. https://doi.org/10.1016/j.rinp.2021.104244.
[56] W. Tan, R. Fu, H. Ji, Y. Kong, Y. Xu, Y. Qin, Preparation of nitrogen-doped carbon using graphene Quantum dots-chitosan as the precursor and its supercapacitive behaviors, International Journal of Biological Macromolecules. 112 (2018) 561–566. https://doi.org/10.1016/j.ijbiomac.2018.02.014.
[57] D.C. Marcano, D.V. Kosynkin, J.M. Berlin, A. Sinitskii, Z. Sun, A. Slesarev, L.B. Alemany, W. Lu, J.M. Tour, Improved Synthesis of Graphene Oxide, ACS Nano. 4 (2010) 4806–4814. https://doi.org/10.1021/nn1006368.
[58] D.C. Marcano, D.V. Kosynkin, J.M. Berlin, A. Sinitskii, Z. Sun, A.S. Slesarev, L.B. Alemany, W. Lu, J.M. Tour, Correction to Improved Synthesis of Graphene Oxide, ACS Nano. 12 (2018) 2078–2078. https://doi.org/10.1021/acsnano.8b00128.
[59] M. Bahdanchyk, M. Hashempour, A. Vicenzo, Evaluation of the operating potential window of electrochemical capacitors, Electrochimica Acta. 332 (2020) 135503. https://doi.org/10.1016/j.electacta.2019.135503.
[60] Y. Chen, L. Chen, H. Bai, L. Li, Graphene oxide–chitosan composite hydrogels as broad-spectrum adsorbents for water purification, J. Mater. Chem. A. 1 (2013) 1992–2001. https://doi.org/10.1039/C2TA00406B.
[61] K. Bustos-Ramírez, A. Martínez-Hernández, G. Martínez-Barrera, M. Icaza, V. Castaño, C. Velasco-Santos, Covalently Bonded Chitosan on Graphene Oxide via Redox Reaction, Materials. 6 (2013) 911–926. https://doi.org/10.3390/ma6030911.
[62] P. Trucano, R. Chen, Structure of graphite by neutron diffraction, Nature. 258 (1975) 136–137. https://doi.org/10.1038/258136a0.
[63] H. Lipson, A.R. Stokes, The Structure of Graphite, Proceedings of the Royal Society A: Mathematical, Physical and Engineering Sciences. 181 (1942) 101–105. https://doi.org/10.1098/rspa.1942.0063.
[64] J. Chen, B. Yao, C. Li, G. Shi, An improved Hummers method for eco-friendly synthesis of graphene oxide, Carbon. 64 (2013) 225–229. https://doi.org/10.1016/j.carbon.2013.07.055.
[65] K. Sakurai, M. Takagi, T. Takahashi, Crystal Structure of Chitosan. I. Unit Cell Parameters, Sen'i Gakkaishi. 40 (1984) T246–T253. https://doi.org/10.2115/fiber.40.7_T246.
[66] K. Sakurai, T. Shibano, K. Kimura, T. Takahashi, Crystal Structure of Chitosan. II. Molecular Packing in Unit Cell of Crystal, Sen'i Gakkaishi. 41 (1985) T361–T368. https://doi.org/10.2115/fiber.41.9_T361.
[67] A.D. French, Idealized powder diffraction patterns for cellulose polymorphs, Cellulose. 21 (2014) 885–896. https://doi.org/10.1007/s10570-013-0030-4.
[68] A. Buléon, P. Colonna, V. Planchot, S. Ball, Starch granules: structure and biosynthesis, International Journal of Biological Macromolecules. 23 (1998) 85–112. https://doi.org/10.1016/S0141-8130(98)00040-3.
[69] A. Imberty, H. Chanzy, S. Pérez, A. Bulèon, V. Tran, The double-helical nature of the crystalline part of A-starch, Journal of Molecular Biology. 201 (1988) 365–378. https://doi.org/10.1016/0022-2836(88)90144-1.
[70] C. Zhang, D.M. Dabbs, L.-M. Liu, I.A. Aksay, R. Car, A. Selloni, Combined Effects of Functional Groups, Lattice Defects, and Edges in the Infrared Spectra of Graphene Oxide, The Journal of Physical Chemistry C. 119 (2015) 18167–18176. https://doi.org/10.1021/acs.jpcc.5b02727.
[71] G. Socrates, Infrared and Raman characteristic group frequencies: tables and charts, 3rd ed., Wiley, Chichester, 2010.
[72] E. Fuente, J.A. Menéndez, M.A. Díez, D. Suárez, M.A. Montes-Morán, Infrared Spectroscopy of Carbon Materials: A Quantum Chemical Study of Model Compounds, The Journal of Physical Chemistry B. 107 (2003) 6350–6359. https://doi.org/10.1021/jp027482g.
[73] B.C. Smith, Infrared spectral interpretation: a systematic approach, CRC Press, Boca Raton, 1999.
[74] J.D.S. Goulden, J.E. Scott, Infrared Frequency and Dissociation Constant of the Carboxylate Group, Nature. 220 (1968) 698. https://doi.org/10.1038/220698a0.
[75] J. Oomens, J.D. Steill, Free Carboxylate Stretching Modes, The Journal of Physical Chemistry A. 112 (2008) 3281–3283. https://doi.org/10.1021/jp801806e.

[76] M. Acik, G. Lee, C. Mattevi, M. Chhowalla, K. Cho, Y.J. Chabal, Unusual infrared-absorption mechanism in thermally reduced graphene oxide, Nature Materials. 9 (2010) 840–845. https://doi.org/10.1038/nmat2858.
[77] A. Bagri, C. Mattevi, M. Acik, Y.J. Chabal, M. Chhowalla, V.B. Shenoy, Structural evolution during the reduction of chemically derived graphene oxide, Nat Chem. 2 (2010) 581–587. https://doi.org/10.1038/nchem.686.
[78] J. Brugnerotto, J. Lizardi, F.M. Goycoolea, W. Argüelles-Monal, J. Desbrières, M. Rinaudo, An infrared investigation in relation with chitin and chitosan characterization, Polymer. 42 (2001) 3569–3580. https://doi.org/10.1016/S0032-3861(00)00713-8.
[79] B. Stuart, Chapter 4. Organic Molecules; 4.5.1 Amines, in: Infrared Spectroscopy: Fundamentals and Applications, Wiley, England, 2004: p. 80.
[80] C.Y. Liang, R.H. Marchessault, Infrared spectra of crystalline polysaccharides. II. Native celluloses in the region from 640 to 1700 cm.1, Journal of Polymer Science. 39 (1959) 269–278. https://doi.org/10.1002/pol.1959.1203913521.
[81] F.G. Hurtubise, Hans. Krassig, Classification of Fine Structural Characteristics in Cellulose by Infared Spectroscopy. Use of Potassium Bromide Pellet Technique, Analytical Chemistry. 32 (1960) 177–181. https://doi.org/10.1021/ac60158a010.
[82] H.G. Higgins, C.M. Stewart, K.J. Harrington, Infrared spectra of cellulose and related polysaccharides, Journal of Polymer Science. 51 (1961) 59–84. https://doi.org/10.1002/pol.1961.1205115505.
[83] K.K. Pandey, A study of chemical structure of soft and hardwood and wood polymers by FTIR spectroscopy, Journal of Applied Polymer Science. 71 (1999) 1969–1975. https://doi.org/10.1002/(SICI)1097-4628(19990321)71:12<1969::AID-APP6>3.0.CO;2-D.
[84] S.Y. Oh, D.I. Yoo, Y. Shin, G. Seo, FTIR analysis of cellulose treated with sodium hydroxide and carbon dioxide, Carbohydrate Research. 340 (2005) 417–428. https://doi.org/10.1016/j.carres.2004.11.027.
[85] B. Soni, E.B. Hassan, B. Mahmoud, Chemical isolation and characterization of different cellulose nanofibers from cotton stalks, Carbohydrate Polymers. 134 (2015) 581–589. https://doi.org/10.1016/j.carbpol.2015.08.031.
[86] S. Krimm, J. Bandekar, Vibrational Spectroscopy and Conformation of Peptides, Polypeptides, and Proteins, in: Advances in Protein Chemistry, Elsevier, 1986: pp. 181–364. https://doi.org/10.1016/S0065-3233(08)60528-8.
[87] J. Hopkins, L. Brenner, C.S. Tumosa, Variation of the Amide I and Amide II peak absorbance ratio in human hair as measured by Fourier transform infrared spectroscopy, Forensic Science International. 50 (1991) 61–65. https://doi.org/10.1016/0379-0738(91)90134-5.
[88] B.R. Singh, D.B. DeOliveira, F.-N. Fu, M.P. Fuller, Fourier transform infrared analysis of amide III bands of proteins for the secondary structure estimation, in: L.A. Nafie, H.H. Mantsch (Eds.), Los Angeles, CA, 1993: pp. 47–55. https://doi.org/10.1117/12.145242.
[89] P. Garidel, H. Schott, Fourier-Transform Midinfrared Spectroscopy for Analysis and Screening of Liquid Protein Formulations Part 2 : Detailed Analysis and Applications, BioProcess International. 4 (2006) 48–55.
[90] L.L. Fernandes, C.X. Resende, D.S. Tavares, G.A. Soares, L.O. Castro, J.M. Granjeiro, Cytocompatibility of chitosan and collagen-chitosan scaffolds for tissue engineering, Polímeros. 21 (2011) 1–6. https://doi.org/10.1590/S0104-14282011005000008.
[91] H. Moussout, H. Ahlafi, M. Aazza, M. Bourakhouadar, Kinetics and mechanism of the thermal degradation of biopolymers chitin and chitosan using thermogravimetric analysis, Polymer Degradation and Stability. 130 (2016) 1–9. https://doi.org/10.1016/j.polymdegradstab.2016.05.016.
[92] R.A. Mauricio-Sánchez, R. Salazar, J.G. Luna-Bárcenas, A. Mendoza-Galván, FTIR spectroscopy studies on the spontaneous neutralization of chitosan acetate films by moisture conditioning, Vibrational Spectroscopy. 94 (2018) 1–6. https://doi.org/10.1016/j.vibspec.2017.10.005.
[93] M. Sekkal, V. Dincq, P. Legrand, J.P. Huvenne, Investigation of the glycosidic linkages in several oligosaccharides using FT-IR and FT Raman spectroscopies, Journal of Molecular Structure. 349 (1995) 349–352. https://doi.org/10.1016/0022-2860(95)08781-P.

[94] M. Kačuráková, M. Mathlouthi, FTIR and laser-Raman spectra of oligosaccharides in water: characterization of the glycosidic bond, Carbohydrate Research. 284 (1996) 145–157. https://doi.org/10.1016/0008-6215(95)00412-2.
[95] N.A. Nikonenko, D.K. Buslov, N.I. Sushko, R.G. Zhbankov, Investigation of stretching vibrations of glycosidic linkages in disaccharides and polysaccarides with use of IR spectra deconvolution, Biopolymers. 57 (2000) 257–262. https://doi.org/10.1002/1097-0282(2000)57:4<257::AID-BIP7>3.0.CO;2-3.
[96] N.A. Nikonenko, D.K. Buslov, N.I. Sushko, R.G. Zhbankov, Analysis of the Structure of Carbohydrates with use of the Regularized Deconvolution Method of Vibrational Spectra, Journal of Balıkesir University, Institute of Science and Technology. 4 (2002) 13–16.
[97] C. Pozo, S. Rodríguez-Llamazares, R. Bouza, L. Barral, J. Castaño, N. Müller, I. Restrepo, Study of the structural order of native starch granules using combined FTIR and XRD analysis, J Polym Res. 25 (2018) 266. https://doi.org/10.1007/s10965-018-1651-y.
[98] M.L. Nelson, R.T. O'Connor, Relation of certain infrared bands to cellulose crystallinity and crystal latticed type. Part I. Spectra of lattice types I, II, III and of amorphous cellulose, Journal of Applied Polymer Science. 8 (1964) 1311–1324. https://doi.org/10.1002/app.1964.070080322.
[99] F.G. Pearson, R.H. Marchessault, C.Y. Liang, Infrared spectra of crystalline polysaccharides. V. Chitin, Journal of Polymer Science. 43 (1960) 101–116. https://doi.org/10.1002/pol.1960.1204314109.
[100] L. Bellamy, The Infra-red Spectra of Complex Molecules, Springer Netherlands, 1975. https://doi.org/10.1007/978-94-011-6017-9.
[101] M.L. Nelson, R.T. O'Connor, Relation of certain infrared bands to cellulose crystallinity and crystal lattice type. Part II. A new infrared ratio for estimation of crystallinity in celluloses I and II, Journal of Applied Polymer Science. 8 (1964) 1325–1341. https://doi.org/10.1002/app.1964.070080323.
[102] A. Bernardino-Nicanor, G. Acosta-García, N. Güemes-Vera, J.L. Montañez-Soto, M. de los Ángeles Vivar-Vera, L. González-Cruz, Fourier transform infrared and Raman spectroscopic study of the effect of the thermal treatment and extraction methods on the characteristics of ayocote bean starches, J Food Sci Technol. 54 (2017) 933–943. https://doi.org/10.1007/s13197-016-2370-1.
[103] A. Imberty, H. Chanzy, S. Perez, A. Buleon, V. Tran, New three-dimensional structure for A-type starch, Macromolecules. 20 (1987) 2634–2636. https://doi.org/10.1021/ma00176a054.
[104] J.J. Cael, J.L. Koenig, J. Blackwell, Infrared and Raman spectroscopy of carbohydrates. Part VI: Normal coordinate analysis of V-amylose, Biopolymers. 14 (1975) 1885–1903. https://doi.org/10.1002/bip.1975.360140909.
[105] F.R. Senti, L.P. Witnauer, Oriented Filaments of Amylose and Alkali Amylose, J. Am. Chem. Soc. 68 (1946) 2407–2408. https://doi.org/10.1021/ja01215a515.
[106] F.R. Senti, L.P. Witnauer, Structure of Alkali Amylose, J. Am. Chem. Soc. 70 (1948) 1438–1444. https://doi.org/10.1021/ja01184a042.
[107] J. Blackwell, A. Sarko, R.H. Marchessault, Chain Conformation in B-amylose, Journal of Molecular Biology. 42 (1969) 379–383. https://doi.org/10.1016/0022-2836(69)90051-5.
[108] H.W. Hsien-Chih, A. Sarko, The double-helical molecular structure of crystalline a-amylose, Carbohydrate Research. 61 (1978) 27–40. https://doi.org/10.1016/S0008-6215(00)84464-X.
[109] H.W. Hsein-Chih, A. Sarko, The double-helical molecular structure of crystalline b-amylose, Carbohydrate Research. 61 (1978) 7–25. https://doi.org/10.1016/S0008-6215(00)84463-8.
[110] K. Chen, S. Song, F. Liu, D. Xue, Structural design of graphene for use in electrochemical energy storage devices, Chem. Soc. Rev. 44 (2015) 6230–6257. https://doi.org/10.1039/C5CS00147A.
[111] X. Liu, Y. Wang, L. Yu, Z. Tong, L. Chen, H. Liu, X. Li, Thermal degradation and stability of starch under different processing conditions, Starch/Stärke. 65 (2013) 48–60. https://doi.org/10.1002/star.201200198.
[112] M.F. El-Kady, V. Strong, S. Dubin, R.B. Kaner, Laser Scribing of High-Performance and Flexible Graphene-Based Electrochemical Capacitors, Science. 335 (2012) 1326–1330. https://doi.org/10.1126/science.1216744.
[113] C. Liu, Z. Yu, D. Neff, A. Zhamu, B.Z. Jang, Graphene-Based Supercapacitor with an Ultrahigh Energy Density, Nano Lett. 10 (2010) 4863–4868. https://doi.org/10.1021/nl102661q.

[114] S. Murali, N. Quarles, L.L. Zhang, J.R. Potts, Z. Tan, Y. Lu, Y. Zhu, R.S. Ruoff, Volumetric capacitance of compressed activated microwave-expanded graphite oxide (a-MEGO) electrodes, Nano Energy. 2 (2013) 764–768. https://doi.org/10.1016/j.nanoen.2013.01.007.
[115] L. Zhang, F. Zhang, X. Yang, G. Long, Y. Wu, T. Zhang, K. Leng, Y. Huang, Y. Ma, A. Yu, Y. Chen, Porous 3D graphene-based bulk materials with exceptional high surface area and excellent conductivity for supercapacitors, Sci Rep. 3 (2013) 1408. https://doi.org/10.1038/srep01408.
[116] Y. Zhu, S. Murali, M.D. Stoller, K.J. Ganesh, W. Cai, P.J. Ferreira, A. Pirkle, R.M. Wallace, K.A. Cychosz, M. Thommes, D. Su, E.A. Stach, R.S. Ruoff, Carbon-Based Supercapacitors Produced by Activation of Graphene, Science. 332 (2011) 1537–1541. https://doi.org/10.1126/science.1200770.
[117] Y. Xu, Z. Lin, X. Zhong, X. Huang, N.O. Weiss, Y. Huang, X. Duan, Holey graphene frameworks for highly efficient capacitive energy storage, Nat Commun. 5 (2014) 4554. https://doi.org/10.1038/ncomms5554.
[118] X. Yang, C. Cheng, Y. Wang, L. Qiu, D. Li, Liquid-Mediated Dense Integration of Graphene Materials for Compact Capacitive Energy Storage, Science. 341 (2013) 534–537. https://doi.org/10.1126/science.1239089.
[119] S.W. Bokhari, A.H. Siddique, P.C. Sherrell, X. Yue, K.M. Karumbaiah, S. Wei, A.V. Ellis, W. Gao, Advances in graphene-based supercapacitor electrodes, Energy Reports. 6 (2020) 2768–2784. https://doi.org/10.1016/j.egyr.2020.10.001.
[120] A. Velasco, Y.K. Ryu, A. Boscá, A. Ladrón-de-Guevara, E. Hunt, J. Zuo, J. Pedrós, F. Calle, J. Martinez, Recent trends in graphene supercapacitors: from large area to microsupercapacitors, Sustainable Energy Fuels. 5 (2021) 1235–1254. https://doi.org/10.1039/D0SE01849J.
[121] W.K. Chee, H.N. Lim, Z. Zainal, N.M. Huang, I. Harrison, Y. Andou, Flexible Graphene-Based Supercapacitors: A Review, J. Phys. Chem. C. 120 (2016) 4153–4172. https://doi.org/10.1021/acs.jpcc.5b10187.
[122] M. He, K. Fic, E. Frąckowiak, P. Novák, E.J. Berg, Ageing phenomena in high-voltage aqueous supercapacitors investigated by in situ gas analysis, Energy Environ. Sci. 9 (2016) 623–633. https://doi.org/10.1039/C5EE02875B.
[123] M.R. Tarasevich, V.A. Bogdanovskaya, N.M. Zagudaeva, Redox reactions of quinones on carbon materials, Journal of Electroanalytical Chemistry and Interfacial Electrochemistry. 223 (1987) 161–169. https://doi.org/10.1016/0022-0728(87)85257-9.
[124] E.C. Peterson, T. Dantzig, Stiffness in fabrics produced by different starches and starch mixtures, and a quantitative method for evaluating stiffness, Technical Bulletins of the United States Department of Agriculture, Economic Research Service. 101 (1929) Technical Bulletin 157334 (formerly No.108) p.1-30. https://doi.org/10.22004/ag.econ.157334.
[125] H.W. Maurer (Ed.), G.G. Bugg, D. Glittenberg, R.L. Kearney, C.P. Klass, A.V. Lyons, S.V. Renvall, Starch and starch products in surface sizing and paper coating, TAPPI Press, Atlanta, GA, US, 2001.
[126] C. Ho, I.D. Raistrick, R.A. Huggins, Application of A-C Techniques to the Study of Lithium Diffusion in Tungsten Trioxide Thin Films, J. Electrochem. Soc. 127 (1980) 343. https://doi.org/10.1149/1.2129668.
[127] E. Barsoukov, J.R. Macdonald, eds., Physical and Electrochemical Models (section 2.2), in: Impedance Spectroscopy: Theory, Experiment, and Applications, 2nd ed, Wiley-Interscience, Hoboken, N.J, 2005: pp. 80–128.
[128] D.C. Grahame, Mathematical Theory of the Faradaic Admittance: Pseudocapacity and Polarization Resistance, J. Electrochem. Soc. 99 (in Fiftieth Anniversary) (1952) 370C. https://doi.org/10.1149/1.2779638.
[129] E. Warburg, Ueber das Verhalten sogenannter unpolarisirbarer Elektroden gegen Wechselstrom, Ann. Phys. Chem. 303 (1899) 493–499. https://doi.org/10.1002/andp.18993030302.
[130] A.J. Bard, L.R. Faulkner, Chap 10; Techniques Based on Concepts of Impedance, in: Electrochemical Methods: Fundamentals and Applications, Wiley, New York, 1980: pp. 368–417.
[131] P.L. Taberna, P. Simon, J.F. Fauvarque, Electrochemical Characteristics and Impedance Spectroscopy Studies of Carbon-Carbon Supercapacitors, Journal of The Electrochemical Society. 150 (2003) A292. https://doi.org/10.1149/1.1543948.
[132] D.R. Dreyer, S. Murali, Y. Zhu, R.S. Ruoff, C.W. Bielawski, Reduction of graphite oxide using alcohols, J. Mater. Chem. 21 (2011) 3443–3447. https://doi.org/10.1039/C0JM02704A.

[133] L. Sun, L. Wang, C. Tian, T. Tan, Y. Xie, K. Shi, M. Li, H. Fu, Nitrogen-doped graphene with high nitrogen level via a one-step hydrothermal reaction of graphene oxide with urea for superior capacitive energy storage, RSC Adv. 2 (2012) 4498. https://doi.org/10.1039/c2ra01367c.
[134] Z. Lei, L. Lu, X.S. Zhao, The electrocapacitive properties of graphene oxide reduced by urea, Energy Environ. Sci. 5 (2012) 6391–6399. https://doi.org/10.1039/C1EE02478G.
[135] Z. Bo, X. Shuai, S. Mao, H. Yang, J. Qian, J. Chen, J. Yan, K. Cen, Green preparation of reduced graphene oxide for sensing and energy storage applications, Sci Rep. 4 (2015) 4684. https://doi.org/10.1038/srep04684.
[136] J.-L. Shi, W.-C. Du, Y.-X. Yin, Y.-G. Guo, L.-J. Wan, Hydrothermal reduction of three-dimensional graphene oxide for binder-free flexible supercapacitors, J. Mater. Chem. A. 2 (2014) 10830. https://doi.org/10.1039/c4ta01547a.
[137] D. Long, W. Li, L. Ling, J. Miyawaki, I. Mochida, S.-H. Yoon, Preparation of Nitrogen-Doped Graphene Sheets by a Combined Chemical and Hydrothermal Reduction of Graphene Oxide, Langmuir. 26 (2010) 16096–16102. https://doi.org/10.1021/la102425a.
[138] H.-L. Guo, P. Su, X. Kang, S.-K. Ning, Synthesis and characterization of nitrogen-doped graphene hydrogels by hydrothermal route with urea as reducing-doping agents, J. Mater. Chem. A. 1 (2013) 2248–2255. https://doi.org/10.1039/C2TA00887D.
[139] S.J. Gregg, K.S.W. Sing, Adsorption, surface area, and porosity, Academic Press, London; New York, 1967.
[140] M. Thommes, K. Kaneko, A.V. Neimark, J.P. Olivier, F. Rodriguez-Reinoso, J. Rouquerol, K.S.W. Sing, Physisorption of gases, with special reference to the evaluation of surface area and pore size distribution (IUPAC Technical Report), Pure and Applied Chemistry. 87 (2015) 1051–1069. https://doi.org/10.1515/pac-2014-1117.
[141] L. Pilon, H. Wang, A. d'Entremont, Recent Advances in Continuum Modeling of Interfacial and Transport Phenomena in Electric Double Layer Capacitors, J. Electrochem. Soc. 162 (2015) A5158–A5178. https://doi.org/10.1149/2.0211505jes.